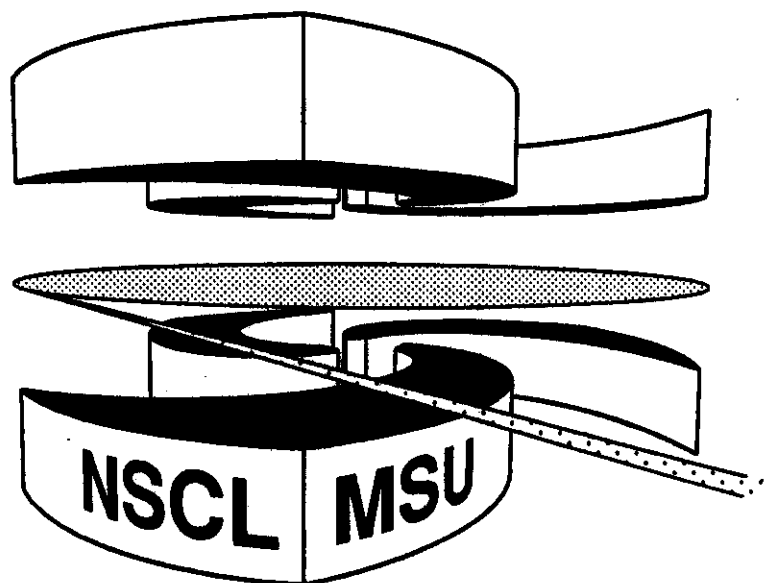# Michigan State University

## National Superconducting Cyclotron Laboratory

# GENERAL ASPECTS OF TRANSPORT THEORY

# IN NUCLEAR PHYSICS

**Lecture given at Interdisciplinary Workshop on "Statistical Description of Transport in Plasma, Astro- and Nuclear Physics," Les Houches, Feb. 2-11, 1993**

## P. DANIELEWICZ

# GENERAL ASPECTS OF TRANSPORT THEORY

# IN NUCLEAR PHYSICS

*P. Danielewicz*

National Superconducting Cyclotron Laboratory and

Department of Physics and Astronomy, Michigan State University,

East Lansing, Michigan 48824, USA

## 1. Introduction

Interest in transport theory in nuclear physics in the last decade has been spurred by the experimental studies of energetic reactions involving heavy nuclei. In these reactions the nuclei are broken up into nucleons and lighter nuclei. New particles, such as gammas and, at higher bombarding energies, $\pi$ and $K$ mesons are produced in collisions. At very high energies quark and gluon degrees of freedom become of importance, but this goes beyond the scope of the talk. Unlike in plasma physics or in different areas of astrophysics, the Wigner phase-space distributions used in the theoretical descriptions of energetic reactions do not merely represent the statistically-averaged pointlike distributions. The distributions generally account for a quantum spread such as for the wavepacket of a single particle.

The dynamics of the reactions is dominated by strong interactions which are also responsible for nuclear binding. The nucleon-nucleon (NN) interactions are attractive at low relative momenta and short-range, $r_{NN} \sim 1\text{fm} = 10^{-15}\text{m}$. The nuclear radius, for comparison, behaves with the nucleon number $A$ as $R \simeq 1.2\text{fm}\,A^{1/3}$. Heaviest nuclei existing in nature have $A$ in the vicinity of 240. The nuclear mass is limited by the repulsive Coulomb interaction which, although weak, is long-range.

Essential for the physics of nuclei and lower-energy reactions is the fact that nucleons are fermions. Pauli principle suppresses NN scattering and in the nuclear ground state the nucleons primarily see an averaged-out potential field of other nucleons of a

depth $V_0 \simeq -50\text{MeV}$.

Energy scales of importance for the reactions are easily deduced. The binding energies of medium and heavy nuclei equal about 8 MeV/nucleon. A complete breakup of the nuclei requires bombarding energies few times in excess of that value. The rest energy for the lightest strongly-interacting particle $\pi$ meson is $m_\pi c^2 \simeq 135\text{MeV}$. These particles start to be produced in significant numbers in collisions at bombarding energies per nucleon few times in excess of their rest energy. Finally, the internal structure of nucleons and mesons starts to play a role at bombarding energies few times in excess of the nucleon rest mass $m_N c^2 \simeq 939\text{MeV} \sim 1\text{GeV}$.

The nucleon Fermi momentum is $p_F \simeq 260\text{MeV/c}$. The momentum combined with the NN interaction-range yields $p_F \, r_{NN} \sim \hbar$. This indicates that in descriptions of reactions the individual NN interactions need to be treated quantally. Though characteristic momenta rise somewhat with the bombarding energy in reactions, the interactions also become inelastic. The inelastic processes as such escape a classical description. The Fermi momentum combined with a radius for medium or heavy nuclei yields on the other hand $p_F R \sim$ few $\hbar$. This indicates the possibility of a classical description of the motion over a nuclear size.

In the past some elaborate methods have been developed for the purpose of understanding the properties of nuclei in their ground-state and in low-lying excited states, such as Brueckner and variational methods. The quantities of interest in theoretical studies included the effective NN interaction in nuclear matter, binding energy per nucleon, and saturation density. Much work has been done on the description of peripheral reactions especially those induced by light projectiles. These so-called direct reactions are typically described in the energy representation. For describing the scattering of nucleons from nuclei a complex optical potential is used, $U = V + iW$. The depth of the real part coincides at low energies with the potential depth for bound nucleons, and the imaginary part is equal to the negative of a half of the rate for scattering with individual nucleons. Nucleon optical potential is also used in describing the central collisions of heavy nuclei.

The many degrees of freedom involved in high-energy reactions, with the multitude of stages, generally force one to use a limited description for the reactions, primarily relying on the single-particle quantities in the time-representation. In my talk I am first going to discuss the general so-called real-time theory concerned with an evolution of physical quantities in a quantum many-body system. Even on a single-particle level the theory is too complex to be directly applied to reactions. However, it provides useful links to the ground-state and direct-reaction theories. Further, within that theory, transport equations may be derived which are simple enough to be practically applied. Conditions for the validity of equations may be analysed and terms in the equations may be given a fundamental basis. In the second part of my talk I shall discuss the transport-theory applications to reactions.

# 2. Many Bodies in Real Time

## 2.1. Perturbative Expansion

Physical quantities are represented by operators. An expectation value at time $t$ is given by

$$< \hat{O}_H(t_1) > = \frac{Tr(\hat{O}_H(t_1)\hat{\rho})}{Tr(\hat{\rho})} = \frac{Tr\left(e^{i\hat{H}(t_1-t_0)}\hat{O}e^{-i\hat{H}(t_1-t_0)}\hat{\rho}\right)}{Tr(\hat{\rho})}$$

$$= \frac{Tr\left(\hat{U}(t_0,t_1)\hat{O}_I\hat{U}(t_1,t_0)\hat{\rho}\right)}{Tr(\hat{\rho})}$$

(1)

where $\hat{O}_H$ is an operator in Heisenberg representation, $\hat{\rho}$ is a density operator that specifies state at time $t_0$, and units are such that $\hbar = 1$. In the expectation value in the Schrödinger or interaction representation the evolution goes forward and then backward in time. Expectation values can be expanded perturbatively in the interaction representation, but track has to be kept not only of the instant at which interaction occurred but also whether interaction occurred during the forward or backward evolution. The easiest way to handle this is by introducing a contour along the time axis going forward and backward, Fig. 1, and defining quantities on the contour. The contour never appears in the consideration of ground-state expectation values or processes in the vacuum, and I shall spend some time explaining the reason.

Following the Gell-Mann-Low theorem, a ground-state, including a relativistic vacuum state, can be obtained from the noninteracting state by adiabatically switching on the interaction, $|\Psi> = \hat{U}(t,-\infty)|\Phi>$. An expectation value of an operator in the ground state becomes then

$$< \Psi|\hat{O}_H(t_1)|\Psi> = < \Phi|\hat{U}(-\infty,t_1)\hat{O}_I(t_1)\hat{U}(t_1,-\infty)|\Phi>$$

$$= < \Phi|\hat{U}(-\infty,+\infty)\hat{U}(+\infty,t_1)\hat{O}_I(t_1)\hat{U}(t_1,-\infty)|\Phi>$$

$$= \frac{< \Phi|\hat{U}(+\infty,t_1)\hat{O}_I(t_1)\hat{U}(t_1,-\infty)|\Phi>}{< \Phi|\hat{U}(+\infty,-\infty)|\Phi>}.$$
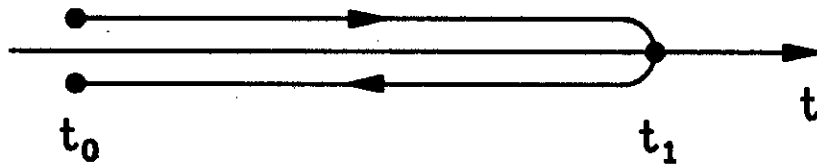
(2)



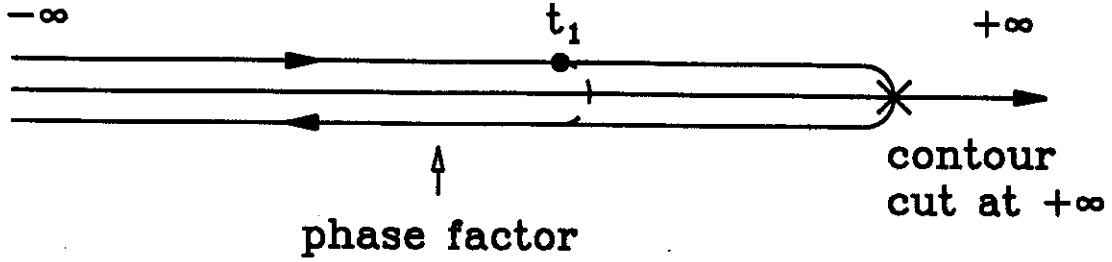Fig. 1. Contour along the time axis for an evaluation of the operator expectation value.

Fig. 2. Calculation of a ground-state expectation value.

The last expression follows from the fact that $\hat{U}(-\infty, +\infty)|\Phi>$ is up to an (infinite) phase factor equal to $|\Phi>$. This enables one to insert a projection operator onto $|\Phi>$ between operators $\hat{U}$ above, and exploit

$$1 = < \Phi|\hat{U}(-\infty, +\infty)|\Phi> < \Phi|\hat{U}(+\infty, -\infty)|\Phi>. \qquad (3)$$

Operations in (2) are illustrated in Fig. 2. In the case of a ground-state expectation value the contour may be elongated to $+\infty$ and cut. In the last expression in (2) the evolution proceeds only forward in time. For $t_1 > t_0$ the evolution operator is

$$\hat{U}(t_1, t_0) = T^c \exp\left(-i \int_{t_0}^{t_1} dt' \hat{H}_I^1(t')\right), \qquad (4)$$

where $\hat{H}_I^1$ is the interaction hamiltonian and $T^c$ a chronological-ordering operator, and, accordingly, the expectation value (2) may be represented as

$$< \Psi|\hat{O}_H(t_1)|\Psi> = \frac{< \Phi|T^c \left[\exp\left(-i \int_{-\infty}^{\infty} dt' \hat{H}_I^1(t')\right) \hat{O}_I(t)\right]|\Phi>}{< \Phi|T^c \left[\exp\left(-i \int_{-\infty}^{\infty} dt' \hat{H}_I^1(t')\right)\right]|\Phi>.} \qquad (5)$$

The r.h.s. may be then expanded in terms of the interaction and further the noninteracting chronological Green's functions,

$$iG_0^c(x, t, x', t') = < \Phi|T^c \left[\hat{\psi}_I(x, t)\hat{\psi}_I^\dagger(x', t')\right]|\Phi>, \qquad (6)$$

using the fact that the expectation value of a product of the interaction-picture field-operators can be represented with a product of the expectation values of pairs of the operators. The result (5) is easily extended to an expectation value of the chronologically ordered product of operators with different time-arguments. Application of the reduction formula to a few-point vacuum chronological Green's function, yields the Feynman-diagram expansion for the scattering matrix.

The above procedure cannot be applied in case of any arbitrary initial state, because the adiabatic switching on and off of the interaction would not return the system to the same state. The evolution proceeding backward in time in (1) must be dealt with directly. For $t_0 < t_1$ the evolution operator is

$$\hat{U}(t_0, t_1) = T^a \exp\left(-i \int_{t_1}^{t_0} dt' \hat{H}_I^1(t')\right),$$  (7)

where $T^a$ is an antichronological ordering operator. The expectation value (1), with (4) and (7), may be written in a compact form upon assigning operators to the sides of the contour in Fig. 1, and introducing an operator $T$ ordering along the contour, generalizing $T^c$ and $T^a$,

$$
\begin{aligned}
< \hat{O}_H(t_1) > =& < T^a \left[ \exp\left(-i \int_{t_1}^{t_0} dt' \hat{H}_I^1(t')\right) \right] \hat{O}_I(t_1) \\
& \times T^c \left[ \exp\left(-i \int_{t_0}^{t_1} dt' \hat{H}_I^1(t')\right) \right] > \\
=& < T \left[ \exp\left(-i \oint_{t_0}^{t_0} dt' \hat{H}_I^1(t')\right) \hat{O}_I(t_1) \right] > .
\end{aligned}
$$  (8)

The time integration in the last expression runs over the contour. The expectation value at time $t_1$ may be then expanded in terms of the interaction and functions defined on the contour,

$$iG_0(x, t, x', t') = < T \left[ \hat{\psi}_I(x, t) \hat{\psi}_I^\dagger(x', t') \right] >,$$  (9)

compare (6).

The result (8) for the operator expectation value is easily extended to the interacting Green's function on the contour

$$
\begin{aligned}
iG(x, t_1, x', t_1') =& < T \left[ \hat{\psi}_H(x, t_1) \hat{\psi}_H^\dagger(x', t_1') \right] > \\
=& < T \left[ \exp\left(-i \oint_{t_0}^{t_0} dt' \hat{H}_I^1(t')\right) \hat{\psi}_I(x, t_1) \hat{\psi}_I^\dagger(x', t_1') \right] >,
\end{aligned}
$$  (10)

that can be expanded in an analogous manner to the expectation value. The contour and Green's functions were first used for the investigation of evolving quantum systems by Schwinger [1] and by Kadanoff and Baym [2], and later by Keldysh [3]. The interacting contour Green's function is useful in carrying out partial resummations in the expansion of expectation values, and it is further of interest on its own. The restriction of the time arguments to specific sides of the contour yields different standard functions. Thus if arguments are restricted to one side of the contour, a chronological or an antichronological function is obtained. These functions generally play the role of propagators in the theory. Two other functions are obtained by restricting the time arguments to the opposite sides of the contour,

$$-iG^<(x, t_1, x', t_1') = < \hat{\psi}_H^\dagger(x', t_1') \hat{\psi}_H(x, t_1) >,$$  (11)

and

$$iG^>(x, t_1, x', t_1') = <\hat{\psi}_H(x, t_1)\hat{\psi}_H^\dagger(x', t_1')> . \tag{12}$$

The function $-iG^<$ reduces to the 1-particle density matrix for equal time-arguments. Thus densities in the configuration space and in momentum space may be obtained from the function. The Fourier transform of the density matrix in relative coordinates yields the Wigner function that corresponds to the classical phase-space density,

$$
\begin{aligned}
f(p; R, T) &= \int dr e^{-ipr} < \hat{\psi}_H^\dagger(R - r/2, T)\hat{\psi}_H(R + r/2, T) > \\
&= \int dr e^{-ipr}(-i)G^<(R + r/2, T, R - r/2, T),
\end{aligned} \tag{13}
$$

While $-iG^<$ represents particles present in the system, the function $iG^>$ is a density for adding particles to the system. In the so-called quasiparticle limit, of low scattering rates, the time structure of the Green's functions contains information about single-particle energies.

In order to illustrate our points let us take the simplest case of a noninteracting uniform system. In this case one finds for the functions Fourier-transformed in relative coordinates,

$$-iG_0^<(p, \omega) = f(p)2\pi\delta(\omega - \omega_p), \tag{14}$$

$$iG_0^>(p, \omega) = (1 - f(p))2\pi\delta(\omega - \omega_p), \tag{15}$$

$$\text{Re}\, G_0^{c,a}(p, \omega) = \frac{\mathcal{P}}{\omega - \omega_p}, \tag{16}$$

where $\omega_p = \frac{p^2}{2m}$.

## 2.2. Green's Function Equations of Motion

The perturbative expansion may be used to derive equations of motion for different 1-particle functions, including the interesting $G^<$, as we shall now show. The equations will have some important consequences.

The different terms in the perturbative expansion are usually illustrated with diagrams in which lines represent Green's functions and points interactions. Lowest-order terms in the expansion of the contour Green's function $G$ in a system with two-body interactions,

$$\hat{H}^1 = \frac{1}{2}\int dx\, dy\, \hat{\psi}^\dagger(x)\hat{\psi}^\dagger(y)V(x - y)\hat{\psi}(y)\hat{\psi}(x), \tag{17}$$

are illustrated in Fig. 3. Generally the functions depend on initial-state correlations indicated in the figure with boxes [4,5]. The perturbative series may be cast into the form of an integral Dyson equation written here schematically

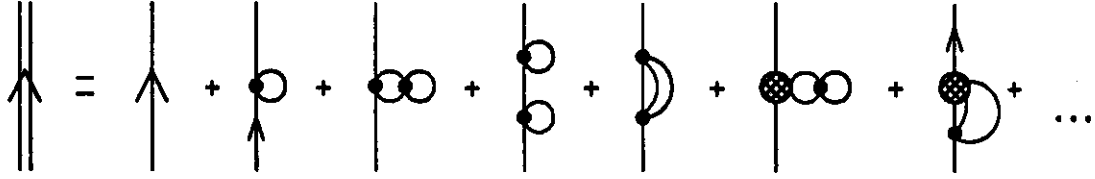$$G = G_0 + G_0\Sigma G, \tag{18}$$

Fig. 3. Expansion of single-particle Green's function.

and illustrated in Fig. 4. The function $\Sigma$ is the self-energy that includes terms which cannot be cut through a single line in the diagrammatic representation, see Fig. 5. We shall drop the effects of initial correlations in the self-energy, assuming $t_0 \to -\infty$. The integral equation may be transformed into a differential equation of motion by introducing the inverse to the noninteracting contour Green's function,

$$G_0^{-1} G_0 = 1. \tag{19}$$

For a nonrelativistic system we find

$$\left( i\frac{\partial}{\partial t} + \frac{\nabla^2}{2m} \right) G_0(\boldsymbol{x}, t, \boldsymbol{x'}, t') = \delta(\boldsymbol{x} - \boldsymbol{x'})\delta(t, t'), \tag{20}$$

with the second $\delta$-function on the r.h.s. defined on the contour in time. Upon applying the inverse Green's function to both sides of (18), we obtain

$$G_0^{-1}G = 1 + \Sigma G, \tag{21}$$

and the equations for $G^<$ and $G^>$ that are known as Kadanoff-Baym equations may be obtained by restricting the time arguments of $G$ in (21) to the opposite sides of the contour. In this way we get for $G^<$

$$
\begin{aligned}
\left( i\frac{\partial}{\partial t} + \frac{\nabla^2}{2m} \right) G^<(t, t') &= \int_{-\infty}^{t} dt_1 (\Sigma^> - \Sigma^<)(t, t_1)G^<(t_1, t') \\
&\quad - \int_{-\infty}^{t'} dt_1 \Sigma(t, t_1)(G^> - G^<)(t_1, t') \\
&= \int_{-\infty}^{\infty} dt_1 \Sigma^+(t, t_1)G^<(t_1, t') + \int_{-\infty}^{\infty} dt_1 \Sigma^<(t, t_1)G^-(t_1, t'),
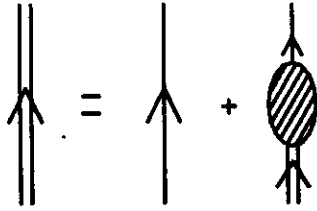\end{aligned} \tag{22}
$$

Fig. 4. Dyson equation.

where time variables are now made explicit. The new functions appearing on the r.h.s. of Eq. (22), so-called advanced and retarded, are defined with

$$G^{\pm}(t,t') = \pm\Theta(\pm(t-t'))(G^{>} - G^{<})(t-t').$$

(23)

Proliferation of functions and the possibility for different representations of expressions is characteristic for nonequilibrium quantum theory. The new Green's functions play a role of propagators in theory, similarly to $G^{c,a}$. The Fourier-transformed noninteracting Green's functions are $G_0^{\pm}(p,\omega) = 1/(\omega - \omega_p \pm i\epsilon)$.

An interpretation to the self-energy $\Sigma^{<}$ may be given, once the equation for $G^{<}$ is solved in a formal manner. From (22) we have

$$(G_0^{-1} - \Sigma^{+})G^{<} = \Sigma^{<}G^{-}.$$

(24)

On combining the equations of motion for $G^{<}$ and $G^{>}$ we get

$$(G_0^{-1} - \Sigma^{+})G^{+} = 1.$$

(25)

With the time variables made explicit we find

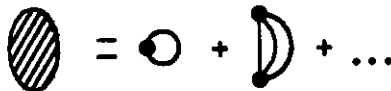$$G^{<}(t,t') = \int dt_1 dt_2 G^{+}(t,t_1)\Sigma^{<}(t_1,t_2)G^{-}(t_2,t').$$

(26)



Fig. 5. Expansion of self energy.

In the above expression $\Sigma^<$ may be interpreted, up to a factor of $-i$, as the source of particles, with $G^\pm$ representing propagation from the source. This interpretation is supported by the representation of the self-energy in terms of the field source $j$, compare (11),

$$-i\Sigma^<(t_1,t_2) = < \hat{j}^\dagger(t_2)\hat{j}(t_1) >_{irr},\tag{27}$$

with $j$ defined by

$$\left(i\frac{\partial}{\partial t} + \frac{\nabla^2}{2m}\right)\hat{\psi} = \hat{j}.\tag{28}$$

In (22) the last term on the r.h.s. corresponds then to production. The self-energy $\Sigma^>$ may be associated with particle absorption,

$$i\Sigma^>(t_1,t_2) = < \hat{j}(t_1)\hat{j}^\dagger(t_2) >_{irr},\tag{29}$$

compare (12), and the self-energy $\Sigma^+$ may be identified with a nonlocal optical potential, cf. (22), consisting of a hermitian and a nonhermitian part,

$$\mathrm{Im}\Sigma^+ = -\frac{1}{2}(i\Sigma^> - i\Sigma^<) = -\frac{1}{2}\Gamma,\tag{30}$$

where $\Gamma$ is hermitian and positive definite.

## 2.3. Thermodynamic Equilibrium

Particularly simple results follow when system reaches a uniform stationary state. In that case the various functions depend only on the differences of time and space variables, and may be Fourier-transformed in these differences. The functions $-i\Sigma^<$ and $i\Sigma^>$ are clearly identified as the production and absorption rates, respectively, of particles with a given momentum. The Kadanoff-Baym equations yield the equality which expresses a balance between the processes of production and absorption,

$$\Sigma^<(p,,\omega)G^>(p,\omega) = \Sigma^>(p,\omega)G^<(p,\omega).\tag{31}$$

As $\Sigma^<$ may be obtained from $\Sigma^>$ by replacing all Green's-function factors $G^<$ with $G^>$ and $G^>$ with $G^<$ [5], it follows that in a stationary system the Green's functions must be related by a factor exponential in the quantities conserved in interactions,

$$G^>(p,\omega) = -e^{\beta(\omega + pv - \mu)}G^<(p,\omega).\tag{32}$$

Further results are obtained after a bit of manipulation. Thus from (26) and (30)-(32) we find, for $v = 0$,

$$-iG^<(p,\omega) = -i\Sigma^<(p,\omega)|G^+(p,\omega)|^2$$
$$= \frac{1}{e^{\beta(\omega-\mu)}+1}\frac{\Gamma(p,\omega)}{(\omega - \frac{p^2}{2m} - \mathrm{Re}\Sigma^+(p,\omega))^2 + \Gamma^2(p,\omega)/4}.\tag{33}$$

The first factor on the r.h.s. is a Fermi-Dirac factor, while the second is the spectral function of a Lorentzian form $A(p, \omega)$. The function $iG^>$ may be expressed in terms of spectral function as

$$iG^>(p, \omega) = \left(1 - \frac{1}{e^{\beta(\omega - \mu)} + 1}\right) A(p, \omega). \tag{34}$$

In the limit of infrequent scattering, the width $\Gamma \to 0$, and the spectral function approaches $A(p, \omega) \to 2\pi\delta(\omega - \omega_p)$. In general, the width function equal to twice the negative of imaginary potential, is related to the real part of potential by a dispersion relation

$$\mathrm{Re}\Sigma^+(\omega) = \Sigma_{HF} + \int \frac{d\omega'}{2\pi} \frac{\Gamma(\omega')}{\omega - \omega'}. \tag{35}$$

## 2.4. Problems with Interpretation

While the real-time theory generates many physically appealing results, there are also numerous cases, typically in the higher order, when expressions obtained within the theory are difficult to interpret. We shall show how these problems can be, in general, resolved.

Let us first illustrate the nature of the problems with the simple result (26). The different Green's functions in the theory are not independent, e.g.

$$G^+ = G^c + G^<, \tag{36}$$

and we could represent the result (26) as

$$G^< = G^+ \Sigma^< G^- = G^c \Sigma^< G^- + G^< \Sigma^< G^-. \tag{37}$$

In the form such as on the r.h.s. the result for $G^<$ could not be given a physical interpretation. In the higher order calculations, in the expansion of the rates $\Sigma^{\lessgtr}$, many different terms appear simultaneously and it is not clear how to manipulate these terms in order to obtain physically understandable results. An intuition from the vacuum would generally suggest the use of chronological functions rather than retarded, but that fails in the example above.

The lowest-order results for the rates are, though, usually easy to understand. I shall first discuss the standard method for calculating the functions, see e.g. Ref. [5]. The contour in Fig. 1 is divided into the chronological and antichronological branches. The external time-arguments, ordered on the contour, are placed on the opposite branches. The Green's functions in the expansion with arguments on the opposite branches are $G^<$ or $G^>$, while those with arguments on one branch are $G^c$ or $G^a$. The functions $G^<$ and $G^>$ represent the densities for the initial and final states in the rates, while functions $G^c$ and $G^a$ contribute to amplitudes multiplying those densities. For the production rate we get in this manner, in the lowest order, in case of the potential interaction

$$-i\Sigma^< = -iv\, iG^< (-i)G^< iG^> iv, \tag{38}$$

Fig. 6. Diagram for self-energy and its representation as a squared amplitude multiplied by densities.

with the respective diagram shown in Fig. 6. In (38) the densities are multiplied by the amplitude $-iv$ and the conjugate amplitude $iv$ as physically expected.

We illustrate the difficulties in the higher order with a meson absorption rate in nuclear medium, calculated in the quasiparticle approximation, assuming well defined particle energies. The lowest-order contribution to the rate, $i\Pi^> \simeq G^> G^<$, illustrated in Fig. 7, can be expected small close to the meson mass shell. Subsequent contributions can be obtained by assigning in different ways the internal vertices of the diagram shown in Fig. 8 to the contour branches, cf. Fig. 9, with the result

$$i\Pi^> = \cdots [G^> G^a D^a G^a G^< \tag{39a}$$
$$+G^> G^< D^< G^> G^< \tag{39b}$$
$$+G^c G^> D^> G^a G^< \tag{39c}$$
$$+G^c G^c D^c G^> G^<]. \tag{39d}$$

In the above $D$ are the meson Green's functions. Integrations and factors for the vertices are suppressed. Interpretation of the expressions (39a) and (39d) is that they account for the vertex corrections in the lowest-order amplitude. In (39c) we recognize densities multiplied by the square of the Compton amplitude. The Compton scattering is expected to contribute to the rate in this order. Problematic is the expression (39b)
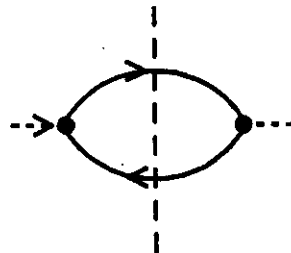


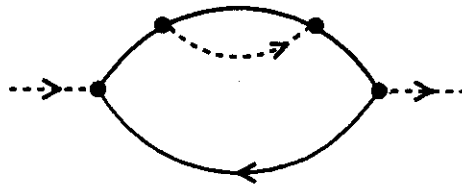Fig. 7. Lowest-order diagram for pion self-energy.

Fig. 8. Higher-order diagram for pion self-energy.

that cannot be identified as a component of a positive-definite rate within a finite order of the perturbation theory. The density product multiplying the 'vacuum-decay' amplitudes in (39b), vanishes in the ground state, as shown below, but not at a finite temperature or in a nonequilibrium situation. Taking a stationary system and the Green's functions Fourier-transformed in relative times, we find that the lines in a diagram running to the isolated vertex of another contour branch, Fig. 9, contribute a factor

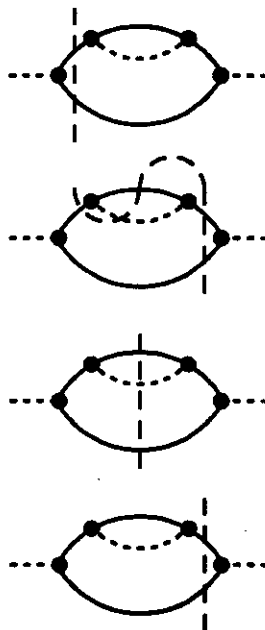$$G^<(\omega - \omega') D^<(\omega') G^>(\omega). \tag{40}$$



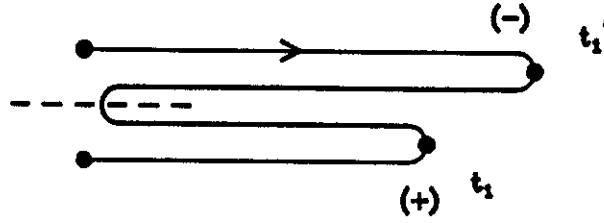Fig. 9. Different ways of cutting the contour diagram from Fig. 8, with a division line between the branches.

Fig. 10. Contour for calculating two-point functions.

In the zero-temperature limit ($\beta \to \infty$) the function $G^<$ vanishes for $\omega - \omega' > \mu$, and the functions $G^>$ and $D^<$ vanish for $\omega' > 0$ and $\omega < \mu$, respectively. This can be seen by examining equilibrium relations between the functions, such as (32), and for the meson functions

$$D^>(\omega) = e^{\beta \omega} D^<(\omega). \tag{41}$$

When examining the equalities above, one finds that the product (40) always vanishes. However, such argument cannot be made in the finite-temperature or nonequilibrium case. An exchange diagram to that shown in Fig. 8 gives rise to similar problems.

## 2.5. Theory in Terms of Retarded Functions

The problems with amplitudes expressed in terms of chronological functions were recognized by DuBois and Bezzerides [6], and by Kobes and Semenoff [7]. A solution was found by myself [8] and independently by Kobes [9]. It consists in using retarded instead of chronological amplitudes. For the purpose of rate calculation the contour may be deformed into one shown in Fig. 10. Then the functions with all vertices on a part of the contour associated with one external time are represented by the retarded amplitudes. The pathological disconnected amplitudes vanish. The result for the meson absorption rate becomes

$$i\Pi^> = \cdots \left[ G^> (GD)^- G^- G^< + G^+ G^> D^> G^- G^< + G^+ (GD)^+ G^> G^< \right], \tag{42}$$

corresponding to the three cuts in Fig. 9 that leave the amplitudes connected. All three terms have clear physical interpretation and can be properly combined with those coming from an exchange diagram to that in Fig. 8. When the retarded amplitudes are being used, the theory becomes explicitly causal. The theory generalizes the vacuum theory outlined in Ref. [10].

Ability to interpret terms in the theory within any order of expansion allows for the introduction of phenomenological amplitudes. It becomes possible to treat processes which are by definition of a high order, such as many-particle interactions and the bound-state production and absorption. In the quasiparticle limit it is found that the single-particle rates may be expanded in the number of interacting quasiparticles
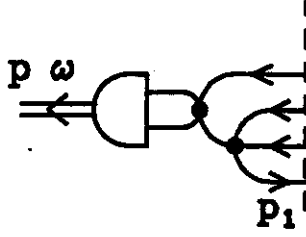
$$\Sigma^> = \Sigma_2^> + \Sigma_3^> + \ldots, \tag{43}$$

Fig. 11. Amplitude for bound-state production.

with

$$i\Sigma_k^>(p,\omega) = \int dp_2 \ldots dp_k \, dp_1' \ldots dp_k' |W^+(p, p_2, \ldots, p_k')|^2$$
$$\times \, \delta(p + p_2 + \ldots + p_k - p_1' - \ldots - p_k')$$
$$\times \, \delta(\omega + \epsilon_2 + \ldots + \epsilon_k - \epsilon_1' - \ldots - \epsilon_k') \quad (44)$$
$$\times \, f_2 \ldots f_k (1 - f_1') \ldots (1 - f_k'),$$

where we suppress powers of $2\pi$. The rate for two-body bound-state production in three-body interactions is found to be of the form

$$iM^<(p,\omega) = \int dp_1 \, dp_1' \, dp_2' \, dp_3' \, |\phi^* W^+|^2 \, \delta(p + p_1 - p_1' - p_2' - p_3')$$
$$\times \, \delta(\omega + \epsilon_1 - \epsilon_1' - \epsilon_2' - \epsilon_3') f_1' f_2' f_3' (1 - f_1), \quad (45)$$

with the amplitude illustrated in Fig. 11.

## 3. Kinetic Theory and Its Validity in Nuclear Reactions

### 3.1. Kinetic Theory

Kinetic theory follows from the real-time theory under the assumption of small temporal and spatial changes in the system. In terms of scattering rates that drive the evolution we must have

$$\Gamma = i\Sigma^> - i\Sigma^< \ll \Omega, \quad (46)$$

where $\Omega$ stands for some characteristic energies. The single-particle functions are Fourier transformed in relative coordinates,

$$G^<(p,\omega,R,T) = \int dr dt \, e^{-i(pr-\omega t)} (-i) G^<(R + r/2, T + t/2, R - r/2, T - t/2), \quad (47)$$

compare (13), and, upon the introduction of transforms into the Kadanoff-Baym equation (25), the equation is expanded in small changes, with $\partial G^</\partial T \sim \Gamma G^<$. In the lowest order we find

$$\left(\omega - \frac{p^2}{2m} - \text{Re}\,\Sigma^+\right) G^< = 0, \qquad (48)$$

i.e.

$$-iG^<(p,\omega,R,T) = f(p,R,T)\,2\pi\delta\left(\omega - \frac{p^2}{2m} - \text{Re}\,\Sigma^+\right). \qquad (49)$$

Within the subsequent order of expansion in the changes, a semiclassical Boltzmann equation is obtained from the Kadanoff-Baym equation,

$$\frac{\partial f}{\partial T} + \frac{\partial \epsilon_p}{\partial p}\frac{\partial f}{\partial R} - \frac{\partial \epsilon_p}{\partial R}\frac{\partial f}{\partial p} = -i\Sigma^<(1-f) - i\Sigma^> f \qquad (50)$$

where $\epsilon_p = p^2/2m + \text{Re}\Sigma^+$. On the l.h.s. of (50) the factor $\partial\epsilon_p/\partial p$ is velocity, the factor $-\partial\epsilon_p/\partial R = -\partial\text{Re}\Sigma^+/\partial R$ is force, and the two terms on the r.h.s. are the gain and loss terms, respectively. The absorption rate associated with a two-body scattering, obtained using (49) and a respective result for $G^>$, becomes

$$i\Sigma^>(p,\omega) = \int dp_1 dp' dp'_1\,\delta(p+p_1-p'-p'_1)\,\delta(\epsilon_p+\epsilon_{p_1}-\epsilon_{p'}-\epsilon_{p'_1})\,|t^+|^2\,f_1(1-f')(1-f'_1).$$
$$(51)$$

The rate $-i\Sigma^<$ has factors $1-f$ replaced by $f$ and conversely.

From the perspective of heavy ion collisions the Boltzmann equation has a definite appeal. The l.h.s. of (50) describes a classical evolution of the phase-space distribution under the influence of the optical potential. The zero-temperature solution to the equation, with the inclusion of finite-range in the potential, corresponds to the Thomas-Fermi approximation often used to describe nuclei. Consequences of the interactions at short distances are described with the squared amplitudes in the collision integral. There are no essential limits on including more involved processes than 2-body scattering in the collision rates, with photon or meson production. However, prior to applying the kinetic theory to reactions, one needs to assess the magnitude of the parameter $\Gamma/\Omega$.

## 3.2. Applicability of Boltzmann Equation to Nuclear Reactions

The damping rate $\Gamma$ is of the order of the absorption rate, when Pauli principle plays negligible role,

$$\Gamma \approx i\Sigma^> \simeq \frac{\hbar}{\tau_f} = \frac{\hbar v}{\lambda} = \hbar n\sigma v, \qquad (52)$$

where $\tau_f$ is the mean free-flight time between collisions, $\lambda$ is mean free path, $v$ - average speed, $\sigma$ - average interaction cross section, and $n$ - density. Taking $\sigma \approx 40\text{mb} = 4\text{fm}^2$, $v \sim 0.8c$, and a normal value for the density $n \approx \frac{1}{7}\text{fm}^{-3}$, we find that $\Gamma \sim 90\text{MeV}$. As the average nucleon energy in the center of mass in symmetric

collisions is, nonrelativistically, $\epsilon = E_{lab}/4A$, the damping rate can be comparable to the c.m. nucleon energies for $E_{lab}/A \lesssim 800\text{MeV}$,

$$\frac{\Gamma}{\epsilon} \sim \frac{1}{2}. \tag{53}$$

Another characteristic energy, stemming from the energy dependence of the self-energies, is $\hbar$ times the inverse of interaction time,

$$\Omega \sim \left| \frac{\Sigma^>}{\frac{\partial \Sigma^>}{\partial \omega}} \right| \lesssim \frac{\hbar v}{r_{NN}}. \tag{54}$$

The condition of the smallness of $\Gamma/\Omega$ becomes purely classical, that of the smallness of the interaction time compared to mean free-flight time or interaction range compared to mean free path, as $\hbar$ drops out,

$$\frac{\Gamma}{\Omega} = \frac{r_{NN}}{\lambda} = r_{NN}\, n\, \sigma \sim \frac{1}{2}. \tag{55}$$

At the late stages of collisions when densities fall, the conditions for the applicability of Boltzmann equation are better satisfied than at the early stages.

### 3.3. Interpenetrating Nuclear Matter Model

Direct comparison of the results from solving the Kadanoff-Baym equations and the Boltzmann equation can be made in the interpenetrating nuclear matter model. The nuclear system is taken as uniform with nucleons in two separated Fermi spheres at the initial time. As the time progresses, the system equilibrates. In the calculation [11] the self-energy was taken in the direct Born approximation with potential parameters fitted to the NN cross section within the Born approximation. Figure 12 shows the evolution of momentum distribution as given by the Boltzmann equation and by the Kadanoff-Baym equations for the uncorrelated and correlated initial state, for the initial separation between Fermi spheres corresponding to $E_{lab}/A = 400\text{MeV}$. Differences between the kinetic and quantum evolutions are observed when $\Gamma/\Omega$ is close to 1. In the momentum distribution from the Boltzmann equation the effects of energy-momentum conservation in binary interactions are seen early on during the evolution. These effects are suppressed in an evolution governed by the Kadanoff-Baym equations. The approach to equilibrium is slower by about 30% in an evolution governed by the Kadanoff-Baym equation than in that governed by the Boltzmann equation.

### 4. Applicability of Hydrodynamics to Nuclear Reactions

If the ideal-fluid hydrodynamics applied to nuclear reactions, the dynamics would be entirely determined by the nuclear equation of state $P = P(n, T)$. The mean free path, $\lambda = 1/n\sigma \simeq 1.8\text{fm}$, is shorter than the radii of heavier nuclei, but the structures such
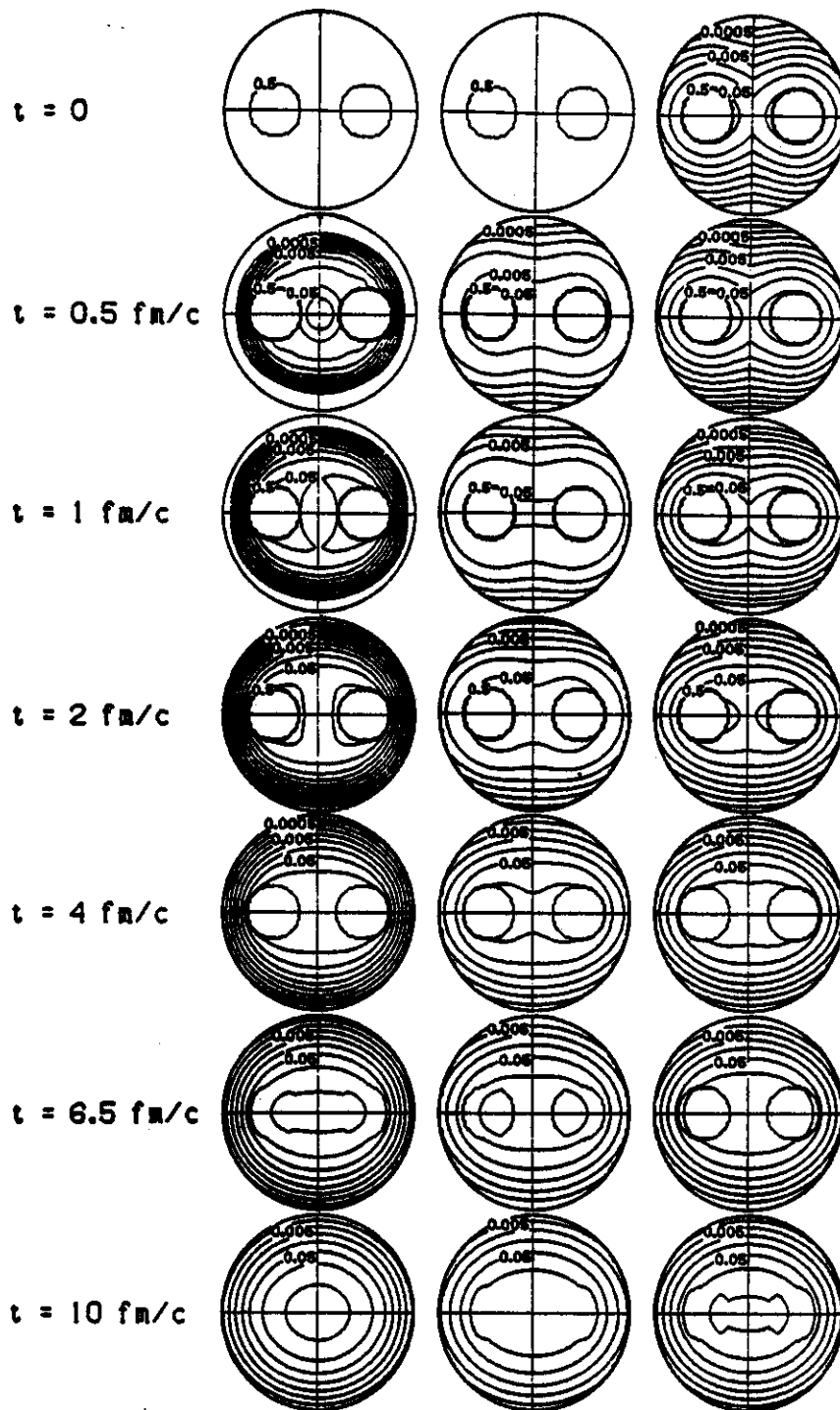
Fig. 12. Contour plots of the evolving nucleon momentum distribution $f(p^{\perp}, p^z, t)$. Leftmost figures - Boltzmann equation evolution; central figures - Green's function equation of motion evolution for a two Fermi-spheres Hartree-Fock initial state; rightmost figures - evolution for a correlated initial state. Horizontal axes are the collision axes. The momentum space is restricted to 900 MeV/c as shown by the outer circles.

as a shock wave, assumed to be of zero width in the hydrodynamics, take more than one mean free path. A shock discontinuity might form in collisions at high energies separating the stopped heated nuclear matter from the incoming cold matter.

In [12] the nuclear-matter shear viscosity and heat conductivity were estimated, and the stationary Navier-Stokes equations were solved for the shock wave profile. The shock width was found to correspond to the equivalent distance in normal nuclear matter of 5 fm at $E_{lab} \gtrsim 200 \text{MeV}/\text{nucleon}$, of the order of the radius of heavier nuclei, and to even greter distances at lower energies. Thus, the ideal-fluid hydrodynamics could not adequately describe the collisions.

The viscous-fluid hydrodynamics might, nevertheless, provide an adequate description, but only for the central regions at intermediate stages of the higher-energy (but presumably not more than 1 GeV/nucleon) reactions. Hydrodynamics necessarily breaks down during the expansion of the system, when $\lambda > 2R$, as $\lambda = 1/n\sigma \propto R^3$, and $R \propto vt$. An uncertainty in the precise specification of the freezout hampers the predictive power of hydrodynamics with respect to the final particle spectra.

The fact that an equilibrium may be reached in the central regions of collisions may offset the inadequacies of the kinetic description in these regions. Once the system finds itself close to an equilibrium, the fine details of dynamics that led to that state cease to matter.


## 5. Transport Description of Nuclear Reactions

Primary objective of the description is to understand the results of collision experiments. The sequence of events in collisions is simulated, with the comparison to data constraining the underlying assumptions. A goal is to assess the properties of dense and excited nuclear matter created in the collisions, and in particular to determine the equation of state of the matter, both at zero and and at a finite temperature. Of interest is whether particles and their interactions are modified in the medium.

Parabolic curves in Fig. 13 indicate the possible behavior of the energy per nucleon in cold nuclear matter, with the variation of density. The nuclei in their ground state correspond to the minimum of energy. As the matter gets compressed in collisions, one expects that the behavior with the density variation can be pinned down using the observables from collisions. A parameter quantifying the stiffness of matter is the compressibility constant $K$, first introduced to characterize the behavior of energy with nuclear radius

$$K = R^2 \frac{d^2}{dR^2} \frac{E}{A} = 9 \, n_0^2 \frac{d^2}{dn^2} \frac{E}{A}. \tag{56}$$

Outside of the nuclear physics, the stiffness is of importance for understanding the mechanism of supernovae explosions. The matter is not only compressed in collisions, but also excited to an energy higher than at zero temperature, by $E^*$, cf. Fig. 13. Following the excitation and compression the matter expands into the vacuum, in a fashion that is most likely isentropic till freezeout. If initial entropy is low, the system may cross the region of instability at densities lower than normal, where $(\partial P/\partial n)_{S/A} < 0$. The dynamics in that region is likely related to the phenomenon of fragmentation
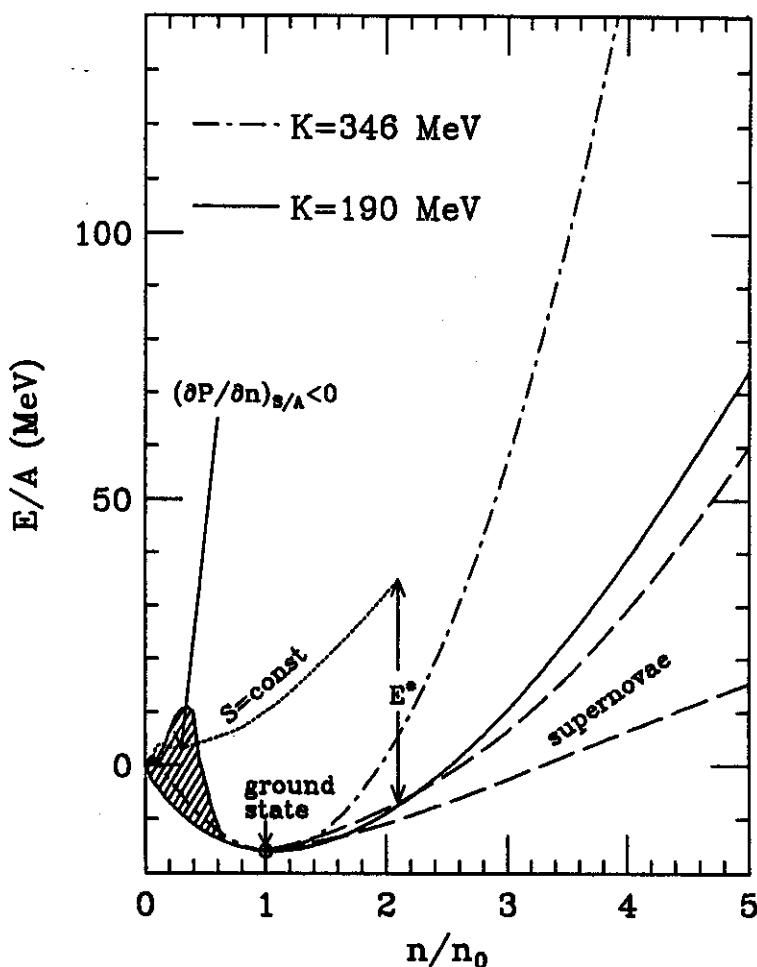
Fig. 13. Energy per nucleon of nuclear matter as a function of density.

discussed in the talks by Randrup and Remaud. Of interest are the growth rates for unstable modes in that region. For low rates close to a critical point, the system may shoot through the region not taking notice of the instability. High growth rates might lead to a violent decomposition.

It should be made clear that in the experiments there is no direct control on the density reached in collisions, excitation energy, degree of equilibration, or other factors. The only existing probes are the emitted particles. Physical description must account simultaneously for many different effects, each with its own uncertainty. Because of the uncertainties, the physical scenarios differing in a particular aspect must frequently differ by as much as 50% in a particular observable, in order to make one scenario more plausible than other, on the basis of comparison to data.

## 5.1. Cascade Model

Essentially all microscopic models used to simulate the high-energy collisions are related to Eq. (50). The simplest microscopic model is the cascade model [13]. In
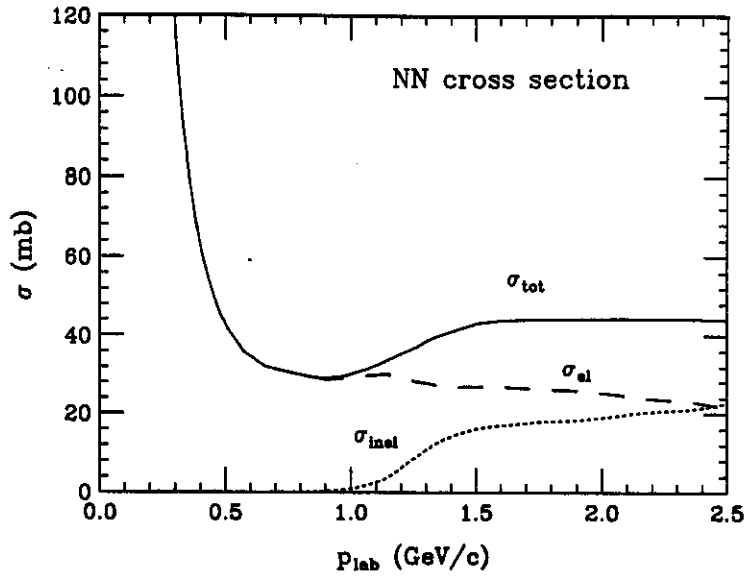
Fig. 14. Nucleon-nucleon cross section as a function of laboratory momentum $(10\text{mb} = 1\text{fm}^2)$.

this model the initial nuclei are treated as a loose collection of nucleons. During the reaction the nucleons collide with the free differential cross sections at higher relative energies, $d\sigma_{NN}/d\Omega \propto |t^+|^2$. The total NN cross section is shown, as function of the laboratory momentum, in Fig. 14. The effects of statistics are ignored in the cascade model. The production of pions is described as a two-step process. First a $\Delta$ resonance, an excited state of a nucleon, is created in a NN collision. The resonance then decays into a nucleon and pion. Experimentally, the $\pi$ production in NN interactions may be primarily attributed to the $\Delta$ resonance excitations up to a bombarding energy of $\sim 2.5\text{GeV}$. Pion absorption may be described with a sequence of inverse processes.

The cascade model has been highly successful in describing the inclusive proton data at high energies, but not at low energies see Fig. 15. The model has consistently overpredicted the pion yields.

## 5.2. Extended Transport Model

From a theoretical standpoint and also from a standpoint of the comparison to data, the description of energetic reactions between heavy nuclei improved considerably upon introducing, by Bertsch, Das Gupta *et al.* [17,18], the effects of the Pauli principle and of the self-consistent optical potential into the transport calculations. Apart from phenomenology, these authors developed numerical methods being widely used.

Phenomenological parametrization of the potential for the transport calculations is conveniently obtained by regarding the total energy as a functional of the distribution function,

$$\epsilon_p(r) = \frac{\delta E}{\delta f(p, r)} = \frac{\delta}{\delta f(p, r)} \left( E^{kin} + E^{pot} \right) = \epsilon_p^{kin} + V(p, r). \qquad (57)$$
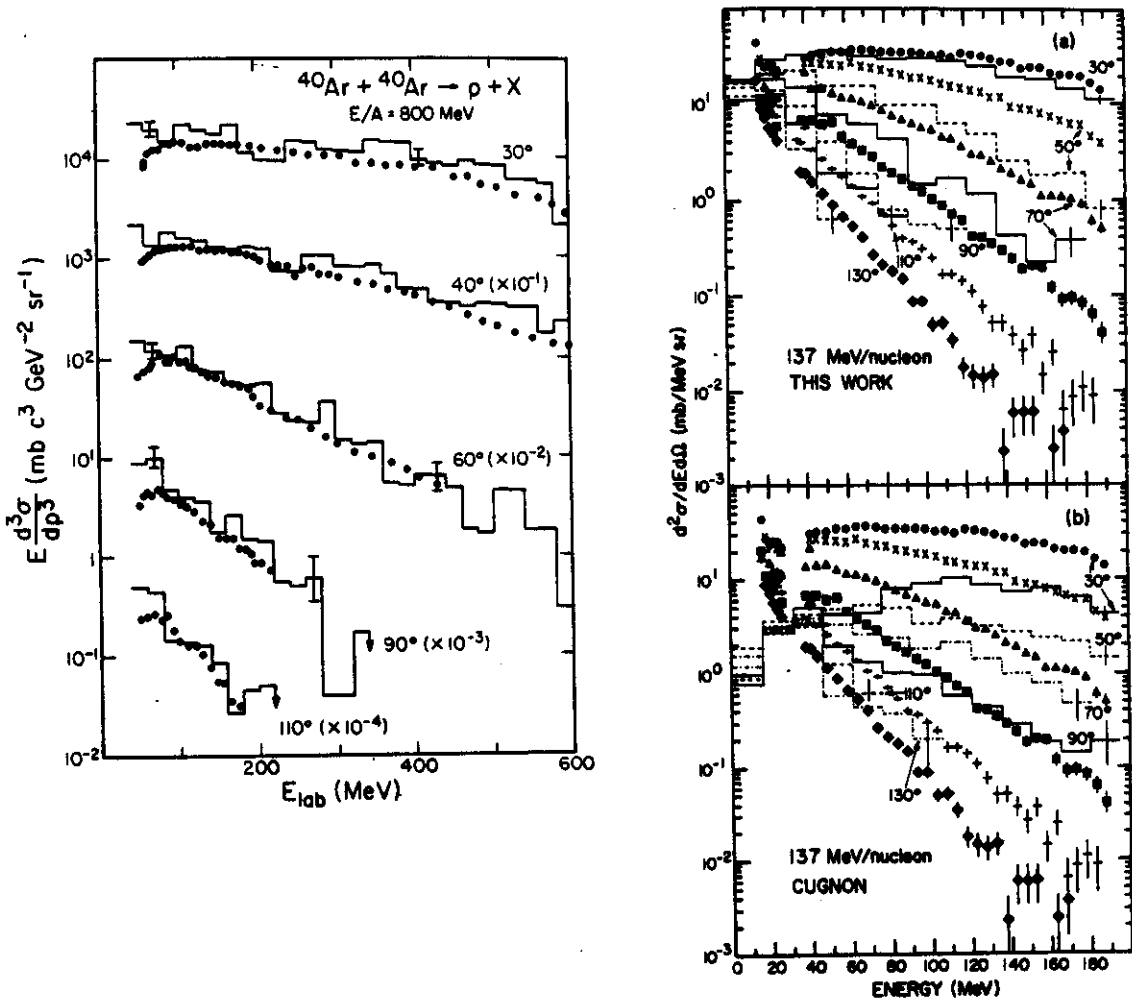
Fig. 15. Inclusive proton spectra measured in the reactions Ar + KCl at 800 MeV/nucleon [14] and Ar + Ca at 137 MeV/nucleon [15], compared to the spectra calculated within the extended transport model [16] (panel marked THIS WORK) and within the cascade model [13] (remaining panels). Data are indicated with points, and calculations with histograms.

The potential energy may be taken in the form

$$E_{pot} \simeq \int dr\, n \left[ \frac{A}{2} \frac{n}{n_0} + \frac{B}{\gamma+1} \left( \frac{n}{n_0} \right)^{\gamma} + \frac{C}{n_0} \int dp \frac{f}{1 + p^2/\Lambda^2} + D\nabla^2 n \right] + E_{coul}, \quad (58)$$

with constants adjusted so that the volume energy has a proper minimum at the normal density, nuclear surface profiles are adequately reproduced within the Thomas-Fermi theory, and the effective mass at the Fermi energy has a desired value. In terms of the constants the potential becomes

$$V = A\frac{n}{n_0} + B \left( \frac{n}{n_0} \right)^{\gamma} + \frac{C}{n_0} \int dp \frac{f}{1 + p^2/\Lambda^2} + C\frac{n}{n_0} \frac{1}{1 + p^2/\Lambda^2} + 2D\nabla^2 n. \quad (59)$$

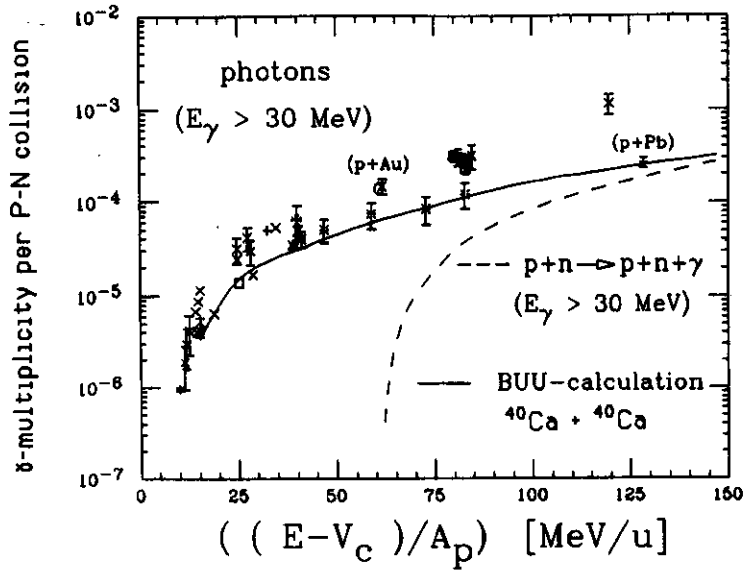Fig. 16. Comparison of the measured and calculated multiplicity of energetic photons ($E_\gamma > 30\text{MeV}$) per primary pn collision [20].

For the discussion of relativistic single-particle energies see Ref. [19]. Figure 15 illustrates the improvement in the description of inclusive data at low energies within an extended transport model, over that in the cascade model.

## 5.3. Gamma Production

Gamma particles serve as a sensitive probe of the reaction dynamics, since they do not interact upon the production. Energetic photons, $E_\gamma \gtrsim 30\text{MeV}$ in lower energy reactions, may be assumed to be produced in independent proton-neutron (pn) collisions when the collisions are infrequent, inhibited by the Pauli principle. (The proton-proton system lacks a dipole moment.) Figure 16 compares the measured multiplicity of energetic photons in various reactions, normalized to the analytically estimated number of first pn collisions, with the multiplicity from the Boltzmann model modified to describe $\gamma$ production [20]. Some degree of an agreement between data and calculation is observed.

## 5.4. Intensity Interferometry

The proton spectra and $\gamma$ multiplicity probe the process of dissipation of the longitudinal motion in the reactions. Space-time dimensions of the emission zone at freezeout may be accessed through the intensity interference.

The technique utilizing pions relies on the fact that the probability density for registering two identical pions with close momenta, $P(p_1, p_2)$, differs from the product of individual probabilities. When the individual probability densities are normalized to 1, the probability for registering two pions coming from points $r_1$ and $r_2$ in the

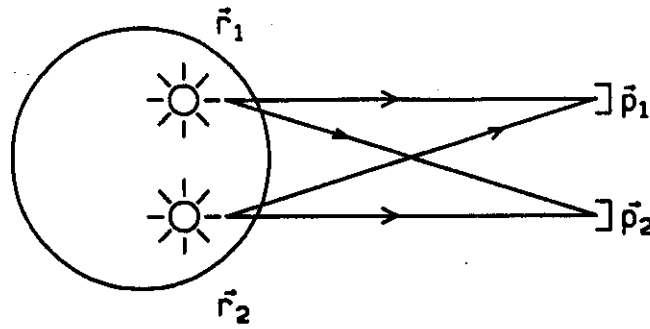Fig. 17. Emission of two identical pions from a source.

source is, cf. Fig. 17,

$$P(\boldsymbol{p}_1, \boldsymbol{p}_2) = \frac{1}{2} \left| e^{i\frac{p_1 r_1}{\hbar}} e^{i\frac{p_2 r_2}{\hbar}} + e^{i\frac{p_1 r_2}{\hbar}} e^{i\frac{p_2 r_1}{\hbar}} \right|^2$$

$$= 2\cos^2 \frac{q(r_1 - r_2)}{2\hbar} = 1 + \cos\left(\frac{q(r_1 - r_2)}{\hbar}\right), \tag{60}$$

where the first equality is due to the symmetrization of wavefunction, as appropriate for Bose statistics, and where $q = \boldsymbol{p}_1 - \boldsymbol{p}_2$. Interaction between two pions is ignored. For $q = 0$ the probability (60) is equal to 2. When $q$ is large the probability $P$, averaged over a range of $r_1 - r_2$, large compared to $q/\hbar$, becomes 1. The drop from 2 to 1 occurs over the range in q of the order of $\hbar/R$, where $R$ is the size of emitting region, Fig. 18.

For a model Gaussian distribution of the emission points used in data parametrizations,

$$S \propto \exp\left(-\frac{r^2}{R^2}\right), \tag{61}$$

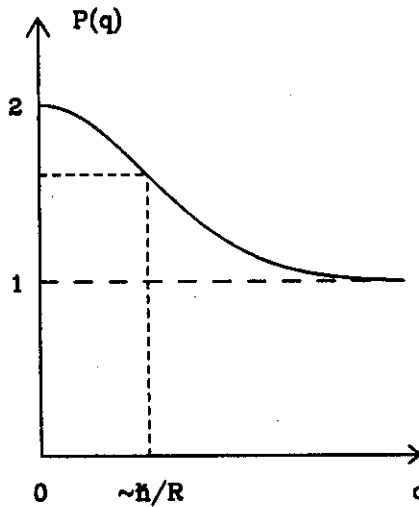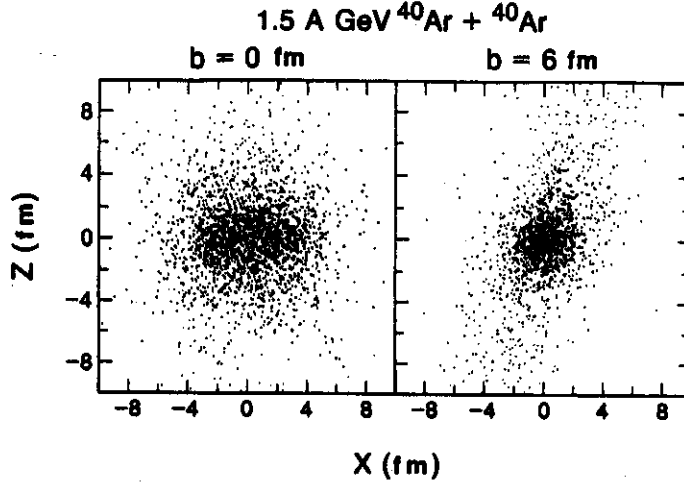

Fig. 18. Probability density $P(q)$.

Fig. 19. Distribution of the pion production points in the Ar + Ar reaction at 1.5 GeV/nucleon [21]. Beam is directed along the z axis.

the 2-pion probability density becomes

$$P(\boldsymbol{p}_1, \boldsymbol{p}_2) = \int d\boldsymbol{r}_1 \int d\boldsymbol{r}_2 S(\boldsymbol{r}_1, \boldsymbol{r}_2) \left[ 1 + \cos\left(\frac{q}{\hbar}(\boldsymbol{r}_1 - \boldsymbol{r}_2)\right) \right] = 1 + \exp\left(-\frac{q^2 R^2}{2\hbar^2}\right). \quad (62)$$

When in addition to the effect of a finite extension in space of the emission, the effect of a finite extension in time is taken into account, with a distribution of emission times taken in a Gaussian form, the result (62) is modified into

$$P = 1 + \exp\left(-\frac{q^2 R^2}{2\hbar^2}\right) \exp\left(-\frac{(E_1 - E_2)^2 \tau^2}{2\hbar^2}\right), \quad (63)$$

where $\tau$ is lifetime.

Figure 19 shows a distribution of the pion production points in the central and peripheral cascade events at bombarding energy of 1.5 GeV/nucleon [21]. Figure 20 compares radii and lifetimes estimated experimentally using parametrization (63) to those obtained within cascade model proceeding through the computation of emission probability from the distribution of production and same parametrization as for the data. Rough agreement between the experimental and calculated results is observed.

Two-pion interferometry is useful at high energies when pions are abundant. At lower energies proton pairs may be used for assessing the dimensions of emission region. While the statistics affects the two-proton probability density, of a relatively greater importance become the interactions between particles moving towards the detectors, Fig. 21. The difference in comparison to the pion case stems from the difference in particle mass. For the same relative momenta of interest, set by the source size, the relative proton energies and velocities are considerably lower than those of pions. In a general case, the probability density for two emission points may be expressed as a square of two-particle scattering wavefunction [22,23], and with the averaging as

$$P(\boldsymbol{p}_1, \boldsymbol{p}_2) = \int d\boldsymbol{r}_1 \int d\boldsymbol{r}_2 S(\boldsymbol{r}_1, \boldsymbol{r}_2) \left| \Psi_{\boldsymbol{p}_1 \boldsymbol{p}_2}(\boldsymbol{r}_1, \boldsymbol{r}_2) \right|^2. \quad (64)$$
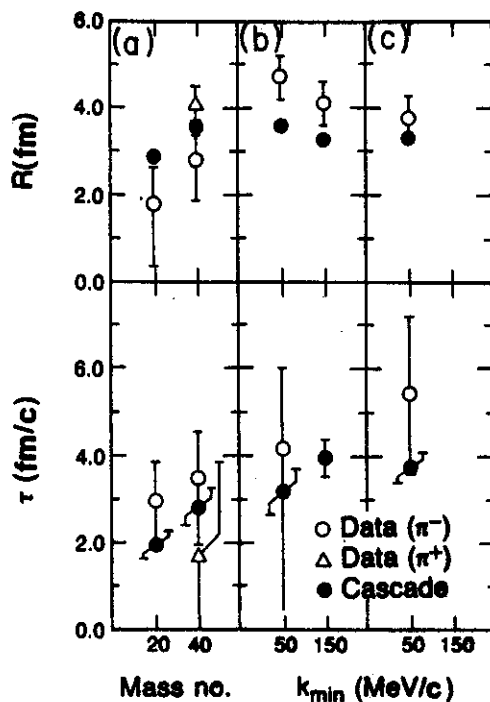
Fig. 20. Comparison [21] between pion source parameters from cascade model and pion interferometry measurements: (a) Ar + KCl and Ne + NaF at 1.8 GeV/nucleon, (b) Ar + KCl at 1.5 GeV/nucleon, (c) Ar + KCl at 1.2 Gev/nucleon.

Figure 22 compares the measured relative probability for detecting protons at a given relative momentum, in the reaction of a nitrogen with aluminum nucleus at 75 MeV/nucleon, to that calculated [24] within the Boltzmann equation model using distribution of points of last scattering [25]. The dip at low momenta is due to the Coulomb repulsion between protons, and the enhancement at higher momenta is due to the attractive nuclear interaction. The structure is more pronounced in the correlation function for high total momenta than for low, indicating that the fast particles are emitted from a smaller source than the slow ones. Semiquantitative agreement between data and calculation is found.
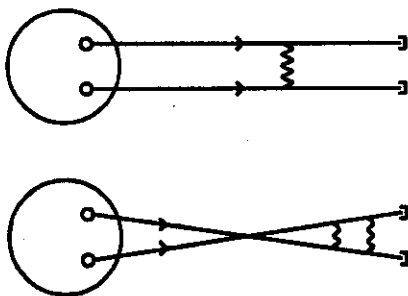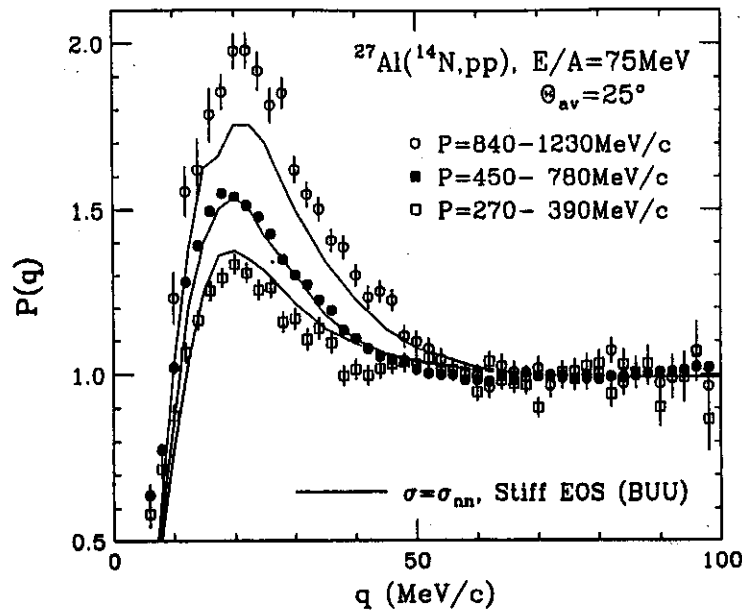


Fig. 21. Two-proton emission.

Fig. 22. Two-proton correlation functions, measured for the collision $^{14}$N$+^{27}$Al at 75 MeV/nucleon, shown by circles and squares, are compared to the predictions of a transport model [24]. Three total momentum gates of the coincidence pair are given.

## 5.5. Collision Dynamics

The rough consistency between various data and final results of transport model calculations, makes plausible the history of the collisions within the model. Figure 23 displays the evolution of the particle distribution in configuration space and momentum space and of a few variables in the Nb + Nb reaction at 1.05 GeV/nucleon [26]. It is seen that, during the initial compression stage, the densities in excess of $2.5n_0$ are reached in the central region. Though it is arguable whether true equilibrium can be reached and the particular system characterized in terms of temperature, the authors have chosen to do so, finding $T$ close to 80 MeV during compression. Most pions are seen to be produced during the initial period. The generated entropy stays essentially constant during the expansion. As to the amount of entropy it may be accessed to some extent experimentally.

If the system were equilibrated, then the entropy could be expressed in terms of the ratio of the chemical potential to temperature

$$S = -\int d\vec{r}d\vec{p}\,(f\log f + (1-f)\log(1-f)) \simeq -\int d\vec{r}d\vec{p}\,(f\log f - f)$$

$$= \int d\vec{r}d\vec{p}\,f\left(-\frac{\mu}{T} + \frac{p^2}{2mT} + 1\right) = A\left(\frac{5}{2} - \frac{\mu}{T}\right).$$

(65)

This ratio is related in equilibrium to the ratio of 2-nucleon clusters deuterons to protons,

$$\frac{N_d}{N_p} \propto \frac{\exp\left(-\frac{2\mu}{T}\right)}{\exp\left(-\frac{\mu}{T}\right)},$$
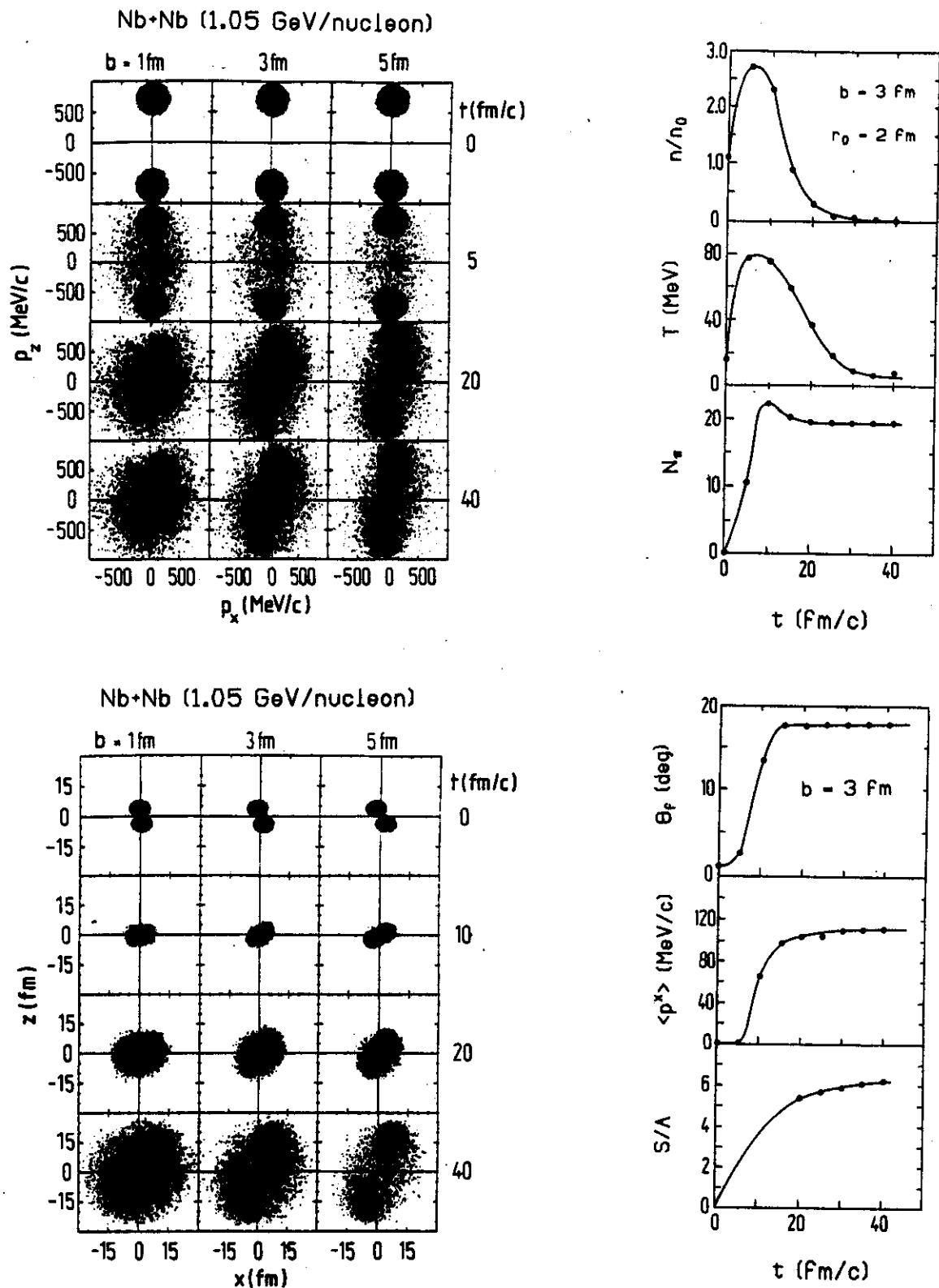
(66)

Fig. 23. Time evolution of the single-particle distributions in configuration and momentum space and of a few variables in the Nb + Nb reaction at 1.05 GeV/nucleon [26].

and finally the entropy per nucleon may be expressed as

$$\frac{S}{A} \simeq 3.9 - \log\frac{N_d}{N_p}.$$

(67)

It may be argued that such a relation as (67) should be also valid outside of equilibrium [27]. The entropy per nucleon estimated experimentally from particle ratios and that calculated in the transport models typically agree within one unit.

As can be seen in Fig. 23, the particles moving forward and backward in the center of mass are on the average deflected sideward during the collision. This can be used to assess the nuclear compressibility.

## 6. Determination of Nuclear Compressibility

### 6.1. Pion Yields and Nuclear Compressibility

An early attempt [28] to determine the nuclear compressibility in the heavy-ion reactions linked the excessive number of pions in the cascade model to the energy needed to compress nuclear matter. Specifically, the reduction in the c.m. energy necessary for making the cascade-model pion multiplicity match the observed multiplicity, Fig. 24, was identified [28] with the change of energy at $T = 0$,

$$\Delta E = E(n) - E(n_0).$$

(68)

With the density taken from the cascade model, a high value of the compressibility constant $K \sim 380\text{MeV}$ was deduced.

It may be mentioned that in a consistent treatment the potential energy $E_{pot}$ should have been used in (68) rather than $E$, leading to a higher value of $K$. (This is because the potential energy is the one missing from the cascade model.) In any case, once the potential energy was incorporated directly into the transport models, a weak sensitivity of the pion multiplicity to the compressibility became apparent [17]. We shall later get back to the pion production and discuss the actual reason for the pion excess in models.

### 6.2. Sideward Flow

Recent attempts were made to determine nuclear compressibility from the sideward deflection such as in Fig. 23. Experimentally the deflection is quantified by evaluating the mean transverse momentum component per nucleon in the reaction plane, as a function of rapidity, Fig. 25. In a nonrelativistic system the rapidity $y$ coincides with the velocity along the beam axis in units of $c$.

General experience from the comparisons to data was following. The cascade model failed to describe data on sideward flow. The transport models with an optical
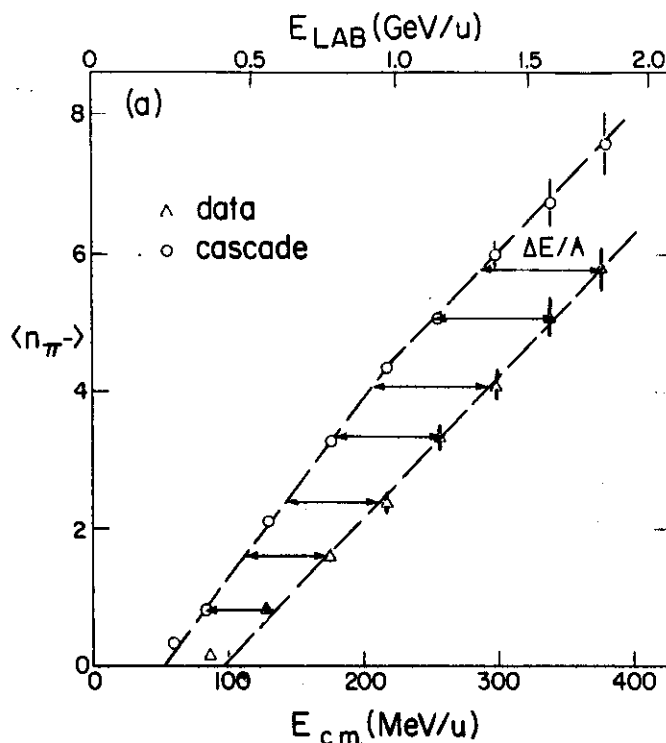
Fig. 24. The mean $\pi^-$ multiplicity as a function of bombarding energy for near-central collisions of $^{40}$Ar + KCl [28]. The triangles show data. Open circles show the results of cascade calculations.

potential $V = V(n)$ could describe the data, if the dependence of potential on density was strong, i.e. $K$ was large. However, from the nucleon-nucleus collisions the optical potential is known to depend also on momentum $p$. When such dependence was incorporated into the model calculations, cf. Eq. (59), it became apparent that data could be described using a potential with a strong momentum dependence and a weak density dependence [30]. With this the situation went into a stalemate. The dependence of potential on momentum was actually never demonstrated in heavy ion collisions.

Quite recently we have been studying with Pan [31] the dependence of flow on the impact parameter for the different parametrizatons of optical potential. In comparisons to data we have used the value of the slope of momentum per mass at midrapidity [29,32], cf. Fig. 25,

$$F = \frac{d < p^x/m >}{dy}\bigg|_{y_0},\qquad (69)$$

in order to avoid the uncertainties associated with fragmentation. Figure 26 compares our slopes to the slopes determined in the Plastic Ball [33] and DIOGENE [32] experiments. Prior to the slope calculation, emitted particles in the model were subjected to detector-acceptance filters. It is seen in the figure that the Plastic Ball data can be described either by using a potential that yields a stiff equation of state and is momentum independent, or by using a potential that yields a soft equation of state but is momentum dependent. This conforms with past experience. Contrasting with
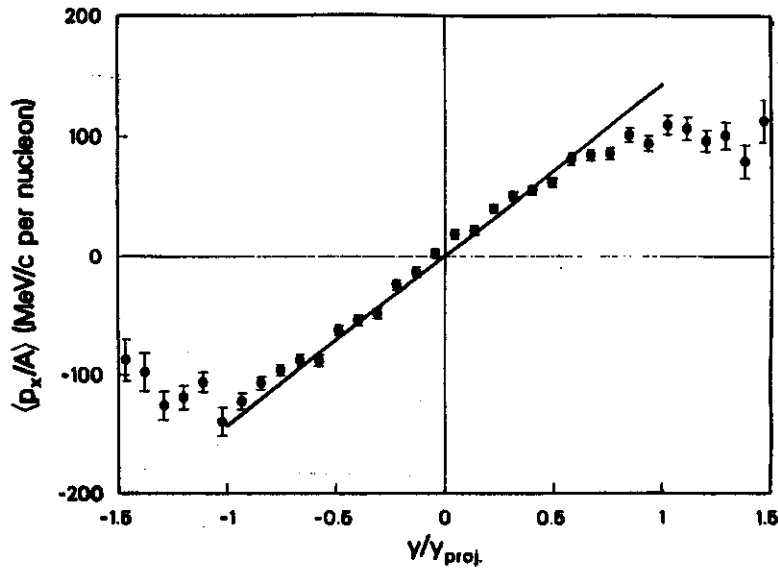
Fig. 25. Mean transverse momentum per nucleon projected onto reaction plane as a function of the normalized center of mass rapidity for Nb + Nb reaction at 400 MeV/nucleon [29].

past experience, however, the DIOGENE data may only be described using a momentum dependent potential. The effect may be understood by examining Fig. 27, and considering detector acceptance. In the figure we show the values of average cosine with respect to the reaction plane as a function of transverse momentum, of the particles emitted in forward rapidity region, for different optical potentials. Predictions differ in the region of high momenta, with particles more focussed in the vicinity of the reaction plane for the momentum dependent than for the momentum independent potentials. The DIOGENE detector setup has poor acceptance for particles emitted with low transverse momenta, while the Plastic Ball setup has good acceptance. Clearly, the poor acceptance enhances the flow values for the momentum dependent relative to the momentum independent potential. Using different sensitivity of the data sets to the density and momentum dependence of optical potential we put [31] limits on compressibility $165\text{MeV} < K < 220\text{MeV}$.

## 7. Pion Production

Let me now concentrate on the issue of the excessive pion number in the cascade and other dynamic models. The resonance $\Delta$, formed in the processes of pion absorption or production in the models, $N + N \leftrightarrow N + \Delta$, $\Delta \leftrightarrow N + \pi$, is fairly broad. It is centered at mass $m_\Delta c^2 = 1232\text{MeV} > (m_N + m_\pi)c^2 = 1077\text{MeV}$, and it has a width of $\Gamma_\Delta \approx 117\text{MeV}$ at $m \simeq m_\Delta$. The spectral function of the resonance

$$A_\Delta(m) = \frac{\Gamma_\Delta}{(m - m_\Delta)^2 + \Gamma_\Delta^2/4}, \tag{70}$$

is illustrated in Fig. 28. In calculating the pion production and absorption rates it has been possible to use data parametrizations for the cross sections $\sigma_{NN \to N\Delta}$ and
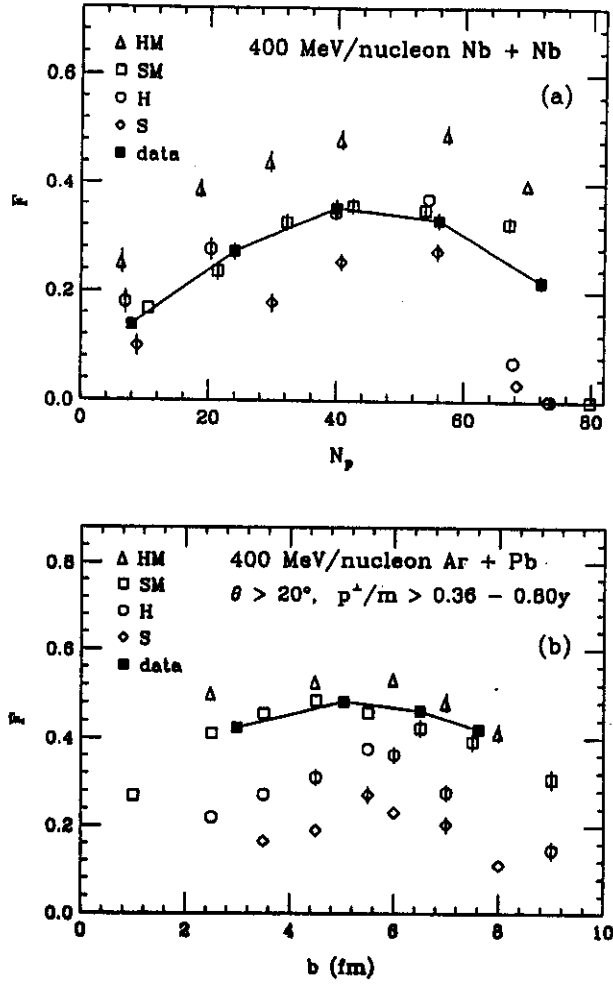
Fig. 26. Flow parameter $F$ in Nb+Nb (a) and Ar+Pb (b) reactions at 400 MeV/nucleon. Data of Refs. [32,33] (filled squares) are compared to the results of calculations [31] for different optical potentials (open symbols). In (a) and (b) the abscissa shows participant proton multiplicity and impact parameter, respectively.

$\sigma_{N\pi\to\Delta}$, as well as for the width. The cross section $\sigma_{N\Delta\to NN}$ had to be deduced from inverse process and the detailed balance relation of a standard form was used,

$$\sigma_{N\Delta\to NN} = \frac{1}{8}\frac{p_{NN}^2}{p_{N\Delta}^2}\sigma_{NN\to N\Delta}. \tag{71}$$

The factor $\frac{1}{8}$ is associated with spin degeneracy and symmetry. In the work [34] with Bertsch, we have determined, however, that relation (71) which would have been valid for stable particles, cannot be used for broad resonances.

The issue is that, in the final-state energy-density for the $\Delta$ production, the spread of $\Delta$ in mass (i.e. equivalently energy) must be included. The spread does not appear, though, in the density for absorption. With $\overline{|\mathcal{M}_{NN\to N\Delta}|^2}$ denoting a squared matrix element for the transition, averaged over spin directions, and the process considered in
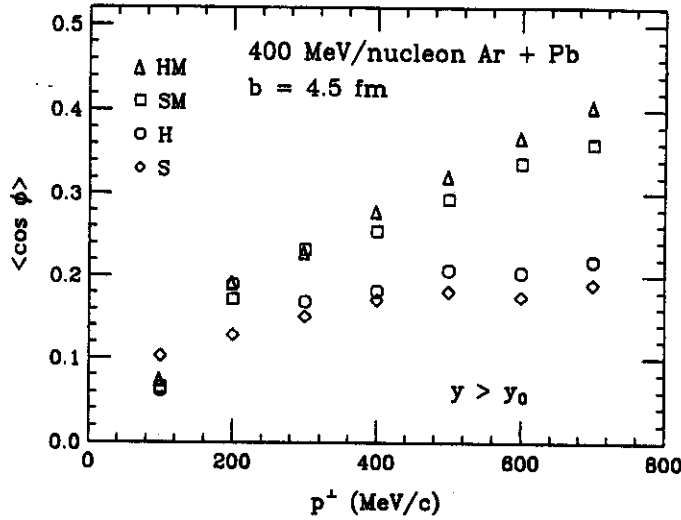
Fig. 27. Mean cosine of the azimuthal angle with respect to the reaction plane, of nucleons emitted at $y > y_0$, as a function of the nucleon transverse momentum.

the center of mass, the $\Delta$-production cross-section takes the form

$$\sigma_{NN \to N\Delta} = \frac{1}{v_{NN}} \int dp_N dp_\Delta dm \overline{|\mathcal{M}_{NN \to N\Delta}|^2} A_\Delta(m) \delta(p_N + p_\Delta) \, \delta(E - \epsilon_N - \epsilon_\Delta). \quad (72)$$

The spin factors and factors of $2\pi$ are suppressed. The $\Delta$-absorption cross-section is, on the other hand

$$\sigma_{N\Delta \to NN} = \frac{1}{v_{N\Delta}} \int dp_{N1} dp_{N2} \overline{|\mathcal{M}_{N\Delta \to NN}|^2} \delta(p_{N1} + p_{N2}) \, \delta(E - \epsilon_{N1} - \epsilon_{N2}). \quad (73)$$

Because of the invariance under time and space reflections, the processes of production absorption share the matrix elements squared,

$$\overline{|\mathcal{M}_{NN \to N\Delta}|^2} = \overline{|\mathcal{M}_{N\Delta \to NN}|^2}. \quad (74)$$

Clearly, by inspection of (71)-(73) and the role of $A_\Delta$, the relation (71) cannot be exactly satisfied when the spectral function is broad. At low energies, such as close to the equilibrium in heavy ion collisions, only a part of the spectral density is integrated
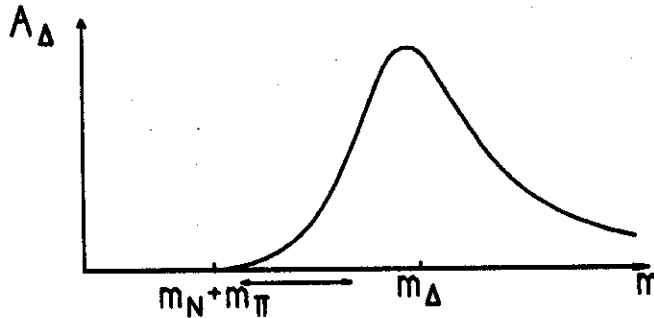


Fig. 28. Spectral function of $\Delta$ resonance.
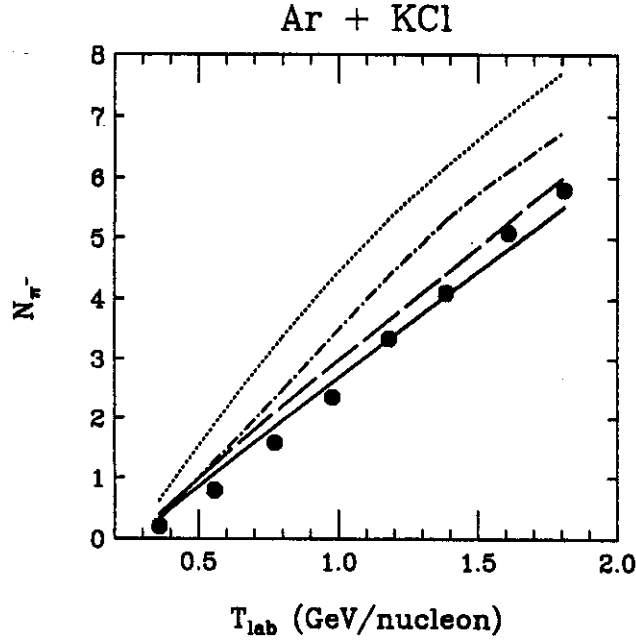
## Ar + KCl



Fig. 29. Negative pion multiplicity as a function of the bombarding energy per nucleon. Dots indicate data of Ref. [35]. The dotted and dash-dotted lines indicate results from the cascade model obtained using the old and new balance relation, respectively. The dashed and solid line indicate results from the Boltzmann equation model obtained using the new detailed balance relation [34].

out in (72), resulting in a reduced production cross section. However, there exists no physical reason for the absorption cross section to be reduced. On the basis of (71) one would conclude that the absorption cross section should be reduced, too. Generally, the resonance absorption is stronger than predicted by (71). On assuming a dependence of matrix element squared on total energy, but not on mass of the produced $\Delta$, a new detailed balance can be derived [34] from (72)-(74),

$$\sigma_{N\Delta \to NN} = \frac{1}{8} \frac{p_{NN}^2}{p_{N\Delta}} \frac{\sigma_{NN \to N\Delta}}{\int^{E-m_N} dm' A_\Delta(m') p'_{N\Delta}}. \tag{75}$$

This relation is consistent with the relations between particle distributions in equilibrium, unlike (71).

Pion multiplicities obtained within cascade model using old and new detailed balance relation are compared in Fig. 29. Even in a relatively light system such as Ar + KCl, the new balance relation reduces by more than 50% the discrepancy between model predictions and data.

It should be mentioned, that while pion multiplicities get under control with the new relation and the inclusion of the mean field and Pauli principle in calculations, this is is not the case with pion spectra. At low c.m. energies an enhancement is observed, similar to that in ultrarelativistic collisions, cf. talk by Bertsch, which transport model fails to describe, see Fig. 30. A discussion of the issue will appear.
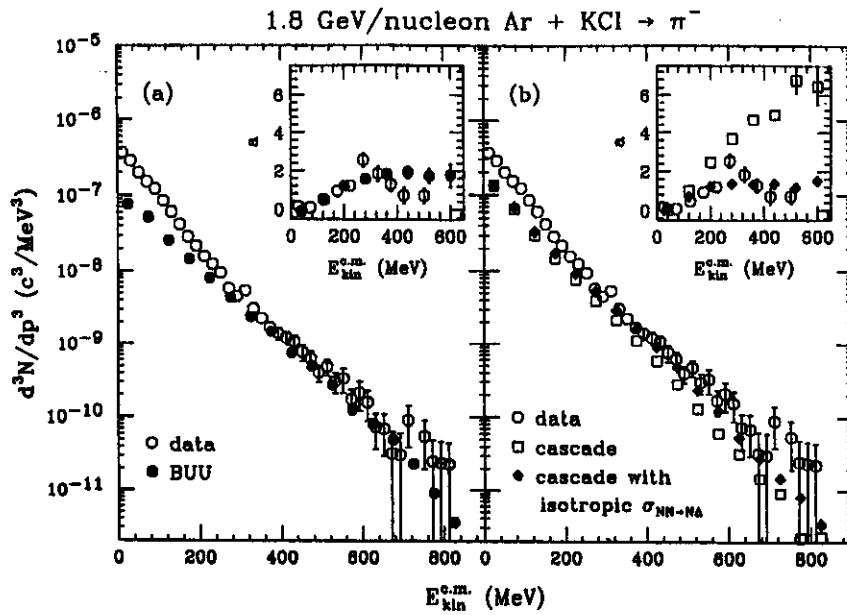
Fig. 30. Comparison of calculated and measured [36] pion energy spectra at c.m. 90° in the Ar+KCl reaction at 1.8GeV/nucleon.

# 8. Beyond the Standard in High-Energy Reactions

## 8.1. Backward Proton Scattering

One of the phenomena that defies the standard description of high-energy reactions as a set of binary collisions, is the phenomenon of backward scattering. When the nuclei are bombarded with high energy protons, and observations are made under a backward angle in the vicinity of 180°, the proton spectrum is found to extend beyond the kinematic limit in the interaction with single nucleon. With the products of binary collisions being focussed forward, sequences of collisions cannot efficiently populate backward momenta. The spectrum extends well beyond the limit of fragmentation as can be seen in Fig. 31. With a rise in the bombarding energy, the spectrum first increases, and then saturates. The data shown correspond to the limiting region of bombarding energies. The spectrum weakly depends on the backward angle.

The saturation of the spectrum and weak dependence on angle suggest that target features play a role. With the kinematics indicating an interaction with more than target nucleon, I have examined [39], as a possible explanation of the phenomenon, the process illustrated in Fig. 32. In the process two target nucleons interact. Thereafter one of the nucleons is emitted and measured, while the other one interacts with the projectile. The last interaction puts the entire process on shell. The rate for backward
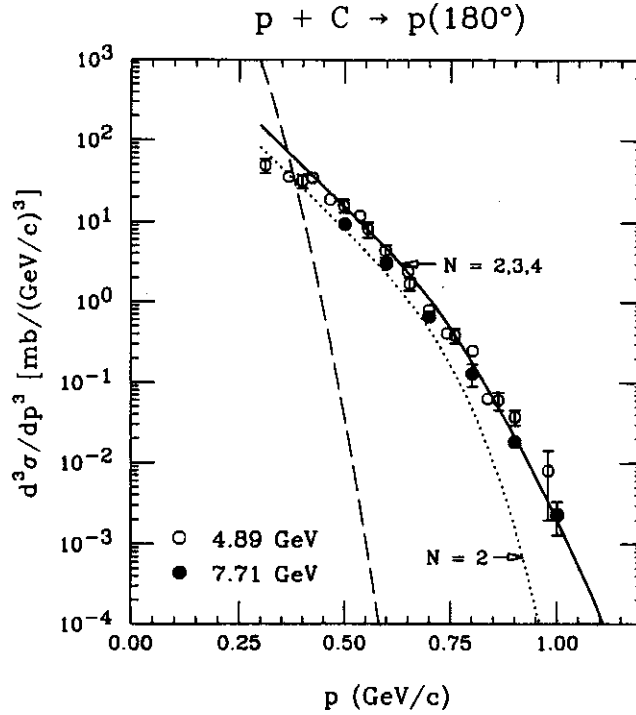
Fig. 31. Cross section for backward proton emission in proton-nucleus interactions. The data are from Refs. [37] (open circles) and [38] (solid circles). Solid line indicates the cross section for emission from the collisions with two, three and four target nucleons. The dotted line indicates the contribution from collisions with two target nucleons. The dashed line represents a rough estimate for maximum contribution to cross section from fragmentation.

production from the process takes the form, cf. (44),

$$
\begin{aligned}
i\Sigma^{>}(p, E) &= \int dp_1 dp_2 d \cdots f(p_1) f(p_2) |t^{+}|^2 \left[ \frac{2m}{(p_1 + p_2 - p)^2 - m^2} \right]^2 |t^{+}|^2 \\
&\quad \times \delta(p^i + p_1 + p_2 - p - \cdots) \delta(E^i + 2(m - B) - E - \cdots) \\
&= \sigma_{NN} \int dp_1 dp_2 f(p_1) f(p_2) |t^{+}|^2 \left[ \frac{2m}{(p_1 + p_2 - p)^2 - m^2} \right]^2 \\
&\quad \times \left( 2(m - B) - p_1^z - p_2^z - E + p^z \right).
\end{aligned}
\tag{76}
$$

The two squared transition matrices in (76) correspond to the two discussed interactions. The functions $f$ are Wigner functions of target nucleons. Dots indicate variables corresponding to unobserved particles in the forward direction. Summation over channels and integration over the momenta of unobserved particles give rise to the NN cross section on the r.h.s. of second equality. The square of the propagator of a nucleon in a virtual state in (76), accounts for the finite time the nucleon can stay off-shell before being struck by projectile. Resulting cross section for the backward emission, obtained by integrating the rate (76) over time and averaging over different straight-line projectile trajectories, is shown in Fig. 31 with a dotted line. Additional contributions to the cross section come from
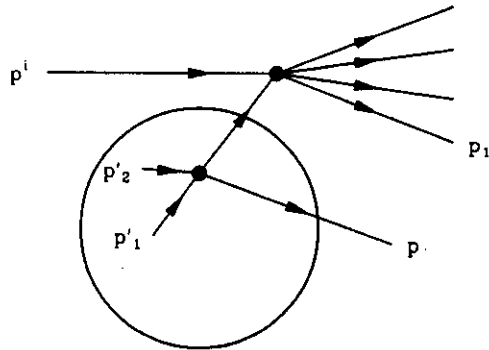
Fig. 32. Collision with two target nucleons.

interactions with more than two target nucleons. The sum is indicated in the figure with a solid line. Probability for finding the second nucleon in the vicinity of the first in (76) is proportional to a local density. Rates for processes with more target nucleons involve additional powers of density. This leads to a rather strong dependence of the backward cross section on target mass, Fig. 33.

## 8.2. Few-Body Collisions in Heavy-Ion Induced Reactions

Unlike in proton-induced reactions at high energies, the sequences of two-body collisions in heavy-ion induced reactions, at lower energies, are expected to populate the edges of single-particle phase space with same efficiency as the few-body collisions. An extensive investigation of the effects of few-body collisions on observables, has been carried out by Batko, Randrup, and Vetter [40].

In their calculation, a two-body collision with a cross section $\sigma$ turned into a three-body collision when a third particle was present [41] within a distance of $\sqrt{\sigma/\pi}$, and into a more-body collision when more particles were present. The available phase space was filled uniformly. At higher energies, when the role of Pauli principle on collisions was diminished, the fraction of few-body collisions in the calculations became quite substantial, see Fig. 34. Despite of that, and despite of different evolution [40], compare Sec. 3.3, the final observables came out very close to the observables from the calculations with 2-body collisions only. This concerned such observables as backward and subthreshold yields, flow variables, and rapidity distributions, cf. Fig. 35. On an opposing end, Bonasera and Gulminelli [42] claim, that the effects of few-body collisions on observables are strong.
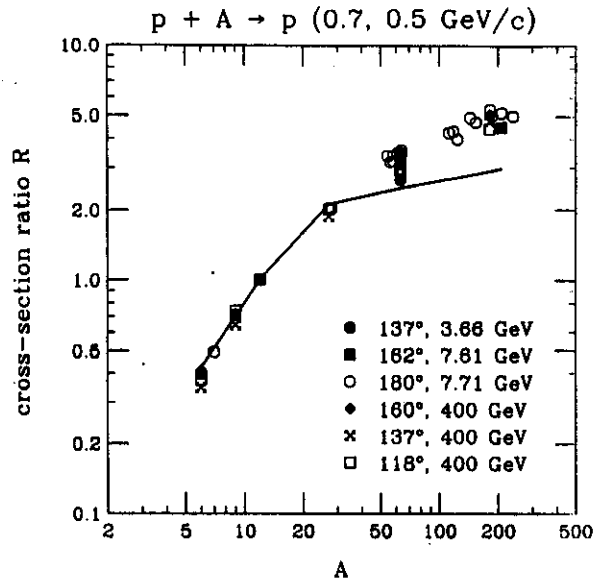
Fig. 33. Cross-section ratio $R = (6/Z)d\sigma(p + A \to p + X)/d\sigma(p +^{12} C \to p + X)$ evaluated from data (symbols) and calculated within the model (line).

## 9. Light Composite Particle Production

### 9.1. Deuteron Transport Equation

As a last topic I shall discuss the production of light composite particles in the energetic nuclear collisions, with deuteron taken as a simplest example. The deuteron Wigner function is related to the 2-nucleon Green's function $G_2^<$. In the limit of low scattering rates the function $G_2^<$ may be represented as [35]
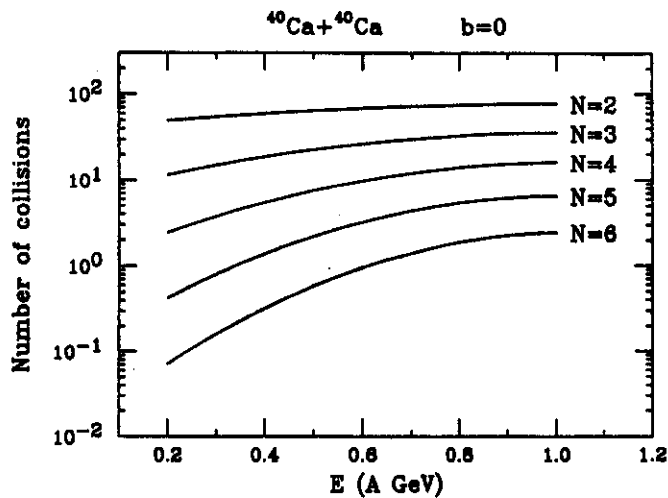


Fig. 34. Beam-energy dependence of the number of N-body collisions in the simulation of Ca+Ca at b=0 [40].
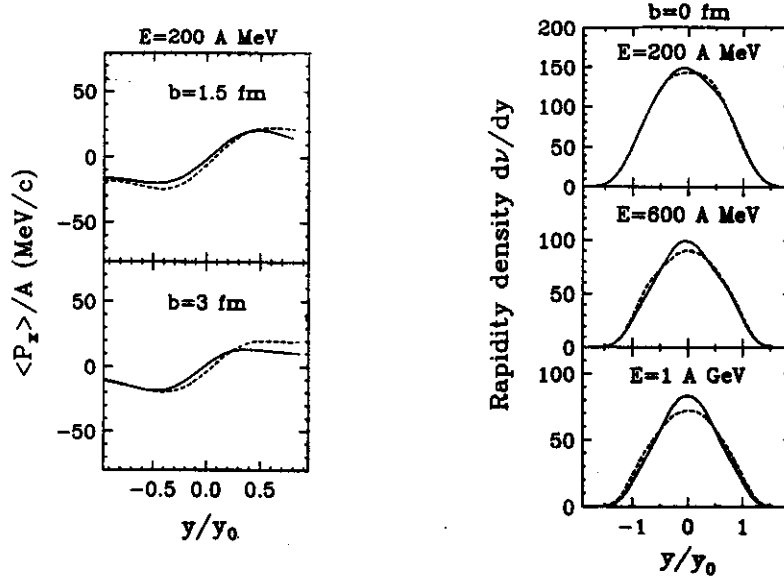
Fig. 35. Average transverse momentum per particle projected onto reaction plane and rapidity density of baryons in Ca+Ca collisions [40]. The dashed lines correspond to standard two-body calculation while the solid lines indicate the results including N-body collisions.

$$
\begin{aligned}
iG_2^< &= < \hat{\psi}_H^\dagger(x_1',t')\hat{\psi}_H^\dagger(x_2',t')\hat{\psi}_H(x_2,t)\hat{\psi}_H(x_1,t) > \\
&\simeq \int dp f_d(p,R,T)\phi_d^*(r')\phi_d(r)\, e^{ip\left(\frac{x_1+x_2}{2}-\frac{x_1'+x_2'}{2}\right)}\, e^{-i\epsilon_d(t-t')} + \dots,
\end{aligned}
\tag{77}
$$

where $R = \frac{1}{4}(x_1 + x_2 + x_1' + x_2')$, $r = x_1 - x_2$, the spin and isospin indices are ignored, $\phi_d$ and $f_d$ are the deuteron internal wavefunction and the Wigner function, respectively, and the dots on the right hand side indicate contributions to the Green's function from 2-nucleon continuum. Equation describing the evolution of deuteron Wigner function follows, in the limit of slow spatial and temporal variations, from the quantum equation for $G_2^<$, and takes the form, compare (50),

$$
\frac{\partial f_d}{\partial T} + \frac{\partial \epsilon_d}{\partial p}\frac{\partial f_d}{\partial R} - \frac{\partial \epsilon_d}{\partial R}\frac{\partial f_d}{\partial p} = \mathcal{K}^< (1 + f_d) - \mathcal{K}^> f_d,
\tag{78}
$$

where $\mathcal{K}^{\lessgtr}$ are deuteron production and absorption rates.

Within the theory [35] it is found that the deuteron rates are related to single particle expectation values,

$$
\mathcal{K}^< = \int dr dr' \phi_d^* v < \hat{\psi}_H^\dagger(x_1',t')\hat{\psi}_H(x_1,t) >< \hat{\psi}_H^\dagger(x_2',t')\hat{\psi}_H(x_2,t) > v\phi_d,
\tag{79}
$$

where $v$ is NN interaction. The absorption rate has the order of operators in the expectation values inverted. In (79) a quasiparticle expansion may be applied. The lowest order, illustrated in Fig. 36(a), corresponds to two nucleons, neutron and proton, joining together and making a deuteron. While this is not possible in the vacuum, the process can, in principle, occur when the nucleons are in a nuclear mean field,
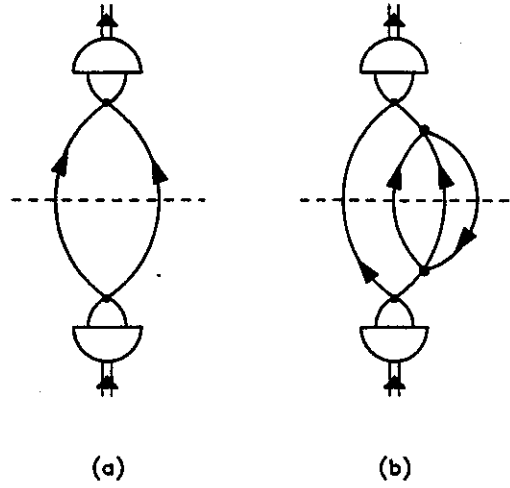
Fig. 36. Expansion of deuteron production and absorption rates.

but the rate is low. Terms of subsequent order in the quasiparticle expansion, Fig. 36(b), correspond to two nucleons colliding, one being then left out as a spectator, and other, still off-shell, joining with a nucleon from vicinity to make a deuteron. When contributions from different processes with three quasiparticles in the initial state, such as just described, are summed up, they give rise to the rate for production of the form, in Wigner representation,

$$
\mathcal{K}^<(\boldsymbol{p}) = \sum_{N=n,p} \int d\boldsymbol{p}_N d\boldsymbol{p}_p d\boldsymbol{p}_n d\boldsymbol{p}'_N \, \overline{|\mathcal{M}^{npN\to Nd}|^2} \delta(\boldsymbol{p} + \boldsymbol{p}_N - \boldsymbol{p}_p - \boldsymbol{p}_n - \boldsymbol{p}'_N)
$$
$$
\times \, \delta(\epsilon_d + \epsilon_N - \epsilon_p - \epsilon_n - \epsilon'_N) f_p f_n f'_N (1 - f_N).
$$
(80)

The average squared matrix element is identical to that for breakup, and is proportional to the differential cross section for breakup, respectively.

The set of equations for nucleons and deuterons yields reasonable wide-angle multiplicities and a good description of spectra in the high-energy collisions of heavy nuclei, see Fig. 37. In [43] the transport description was extended to include the $A = 3$ fragments.

## 9.2. Effects of Transverse Expansion

In the transport simulations of the head-on collisions at bombarding energies of the order of few hundred MeV, carried out with Pan [43], we found that a region with dense and excited matter in the center between nuclei, expands with time predominantly in transverse directions. According to simulations, the energies and angular distributions of emitted light fragments could be used to identify and quantify the transverse expansion.

Figure 38 shows the evolution of the density of particles projected onto the reaction plane, in the Au+Au collisions at 250 MeV/nucleon. The transverse expansion is clearly seen. Figure 39 shows the measured [44] and calculated mean energies of light fragments emitted towards 90° in the center of mass in the collisions. The energies
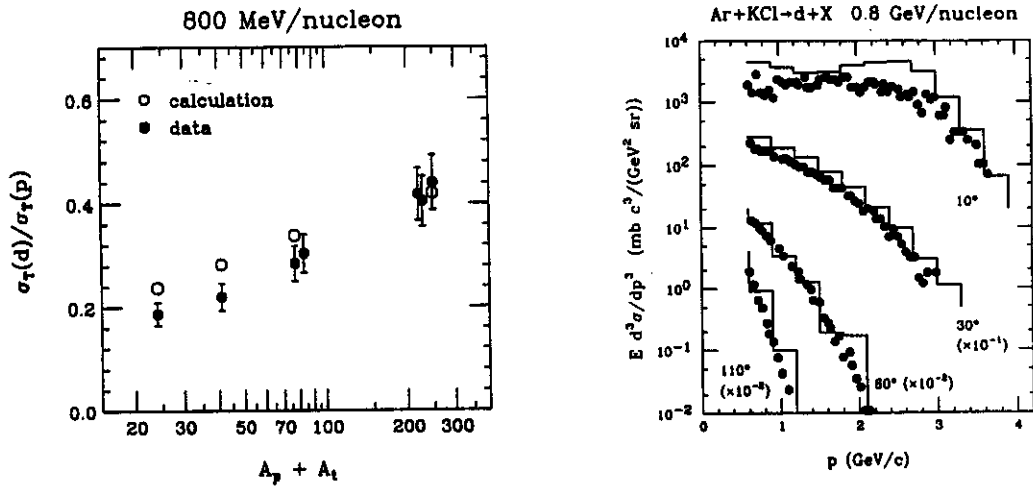
Fig. 37. Ratio of deuteron to proton yields in 800MeV/nucleon reactions, and deuteron spectrum from 800 MeV/nucleon Ar+KCl reaction. Abscissa for the ratio is the sum of projectile and target masses. Calculated spectrum is indicated with a histogram, and measured spectrum with points. The data are from Ref. [14].

rise with decreasing impact parameter. The transverse proton energies in the very central collisions exceed, in fact, the energy per nucleon available in the center of mass. Besides the rise of energies, significant differences between energies of various fragments develop with decreasing $b$. Within the simulation we can analyze in detail the origin of differences. We find that, prior to a freezeout, a local equilibrium is established in the collisions, and differences between energies of fragments with different mass are due to the expansion,
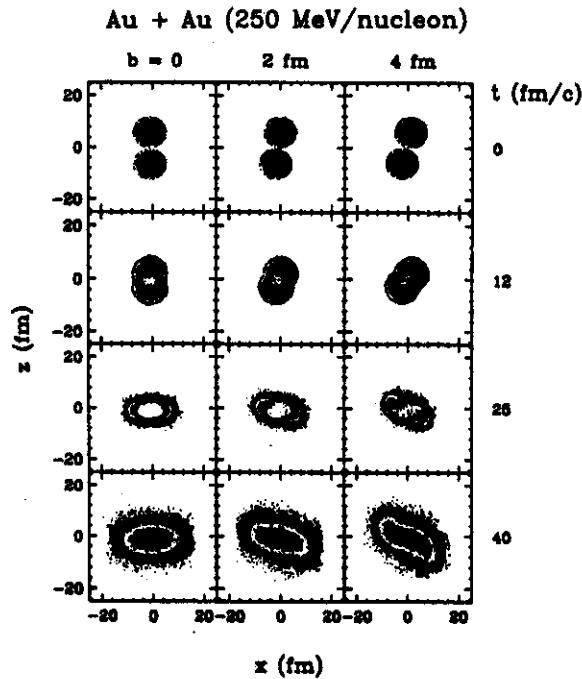


Fig. 38. Contour plots of particle density integrated over the normal to reaction plane in Au+Au collisions at 250MeV/nucleon.
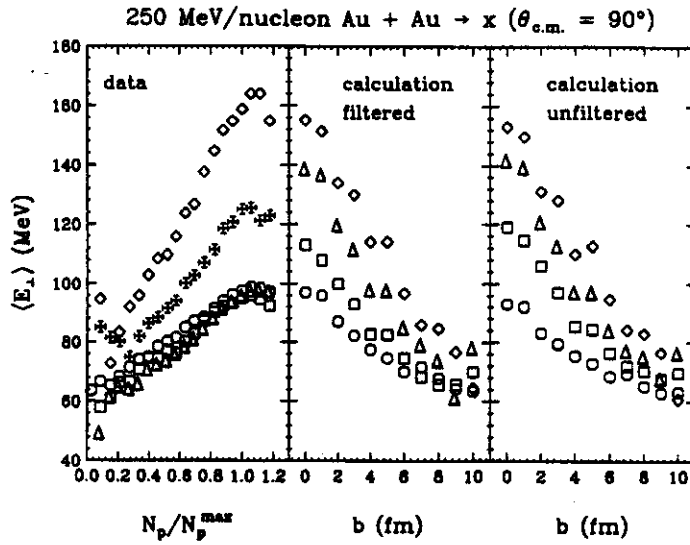
250 MeV/nucleon Au + Au → x ($\theta_{c.m.}$ = 90°)



Fig. 39. Mean kinetic energies of protons (circles), deuterons (squares), triton-s (triangles), helions (diamonds), and alphas (crosses) in the Au+Au collisions at 250MeV/nucleon. Left panel displays energies determined in the experiment of Ref. [44]. Center and right panels show the results of calculation [43] as a function of impact parameter in the direct form, and with the final state subjected to a procedure simulating detector acceptance, respectively.

$$< E >_{90°} = \frac{3}{2}\frac{m < v_\perp^2 >}{2} + \frac{3}{2}T = \frac{3}{2}A\frac{m_N < v_\perp^2 >}{2} + \frac{3}{2}T = \frac{3}{2}AE_{\perp N}^{coll} + \frac{3}{2}T. \quad (81)$$

Additional differences between fragments with different charge develop when fragments move away from the reaction region, due to Coulomb interaction. When comparing our results to data [44], consistency is found for the proton and helion energies, but not for the triton and deuteron energies. Two new data sets are being analyzed right now, hopefully shedding more light on the situation.

## 10. Conclusion

Let me conclude by listing few interesting open problems. For one, it is important to find out whether the results on equation of state can be confirmed by other researchers. If this were the case, possibilities for a direct investigation in the experiment of the effects of momentum dependence would be open, and possibly features of the equation could be more narrowed down. With a strong momentum dependence, the issues of rate renormalization may need, finally, be dealt with seriously, even at high energies.

The mechanism of fragmentation still remains open. An interesting new quantal approach with fluctuations, that may describe adequately some physics, is the Fermion Molecular Dynamics. Analysis of data on fragmentation could benefit from variables identifying a critical behavior.

The low-momentum enhancement in pionic spectra represents a mystery. A peak is observed in the spectra at low and high energies, and further in heavier and lighter

systems, where, supposedly, the dynamics should be different. Possibly related in some way to the peak is the issue of virtual vs classical propagation of the $\Delta$ resonances. Well below the center of the resonance, the time for $\Delta$ existence becomes limited by the uncertainty principle. Generally, transport involving virtual particles may be of essence at very high energies, since particles can live macroscopic times due to the Lorentz dilation.

Concerning few-particle interactions, interesting are new data on antiproton production in proton-nucleus and deuteron-nucleus reactions. Yields differ by factor of 50 in the subthreshold region, and the standard models can explain only difference by a factor $\sim 5$ [45].

As to the general quantum nonequilibrium theory, of importance is solving the problem of a simultaneous renormalization of the amplitudes and densities, with a regard to conservation laws. Densities need to be formulated for transient stages of dynamics when neither asymptotic states cannot be used, nor features of a stationary limit can be exploited.

## 11. Acknowledgement

### REFERENCES

[1] J. Schwinger, *J. Math. Phys.* **2** (1961) 407.
[2] L. P. Kadanoff and G. Baym, *Quantum Statistical Mechanics* (Dover, New York, 1962).
[3] L. V. Keldysh, *ZhETF* **47** (1964) 1515.
[4] A. G. Hall, *J. Phys.* **A8** (1975) 214;
P. Henning, *Nucl. Phys.* **B337** (1990) 547.
[5] P. Danielewicz, *Ann. Phys. (N.Y.)* **152** (1984) 239.
[6] D. F. DuBois, in: *Lectures in Theoretical Physics*, ed. W. E. Brittin, Vol. IXC (Gordon & Breach, New York, 1967) p. 496;
B. Bezzerides and D. F. DuBois, *Phys. Rev.* **168** (1968) 233.
[7] R. L. Kobes and G. W. Semenoff, *Nucl. Phys.* **B260** (1985) 714;
*ibid.* **B272** (1986) 329.
[8] P. Danielewicz, *Ann. Phys. (N.Y.)* **197** (1990) 154.
[9] R. Kobes, *Phys. Rev.* **D43** (1991) 1269.
[10] F. Dyson, *Phys. Rev.* **82** (1951) 428.
[11] P. Danielewicz, *Ann. Phys. (N.Y.)* **152** (1984) 305.
[12] P. Danielewicz, *Phys. Lett.* **B 146** (1984) 168.
[13] Y. Yariv and Z. Frankel, *Phys. Rev.* **C 20** (1979) 2227;
C. Cugnon, *ibid.* **22** (1980) 1885.
[14] S. Nagamiya *et al.*, *Phys. Rev.* **C 24** (1981) 971.

[15] B. V. Jacak *et al.*, *Phys. Rev. Lett.* **51** (1984) 1846.

[16] H. Kruse *et al.*, *Phys. Rev. C* **31** (1985) 1770.

[17] G. F. Bertsch, S. Das Gupta, and H. Kruse, *Phys. Rev. C* **29** (1984) 673.

[18] G. F. Bertsch and S. Das Gupta, *Phys. Rep.* **160** (1988) 189.

[19] G. Baym and S.A. Chin, *Nucl. Phys.* **A262** (1976) 527.

[20] W. Cassing *et al.*, *Phys. Rep.* **188** (1990) 363.

[21] T. Humanic, *Phys. Rev. C* **34** (1986) 191.

[22] S. E. Koonin, *Phys. Lett. B* **70** (1977) 43.

[23] D. H. Boal, C. K. Gelbke, and B. K. Jennings, *Rev. Mod. Phys.* **62** (1990) 553.

[24] W. G. Gong *et al.*, *Phys. Rev. C* **47** (1993) R429.

[25] P. Danielewicz and P. Schuck, *Phys. Lett. B* **274** (1992) 268.

[26] J. J. Molitoris, H. Stöcker, and B. L. Winer, *Phys. Rev. C* **36** (1987) 220.

[27] P. J. Siemens and J. I. Kapusta, *Phys. Rev. Lett.* **43** (1979) 1690;
     G. Bertsch and J. Cugnon, *Phys. Rev C* **24** (1981) 2514.

[28] R. Stock *et al.*, *Phys. Rev. Lett.* **49** (1982) 1236.

[29] K. G. R. Doss *et al.*, *Phys. Rev. Lett.* **57** (1986) 302.

[30] C. Gale *et al.*, *Phys. Rev. C* **35** (1987) 1666;
     J. Aichelin *et al.*, *Phys. Rev. Lett.* **58** (1987) 1926.

[31] Q. Pan and P. Danielewicz, *Phys. Rev. Lett.* **70** (1993) 2062.

[32] M. Demoulins, Ph. D. Thesis, University Paris Sud, 1989 [CEN Saclay Report
     No. CEA-N-2628, 1990];
     J. Gosset *et al.*, in *The Nuclear Equation of State,* edited by W. Greiner and H.
     Stöcker, *NATO ASI Ser. A* **216**, (Plenum, New York, 1989) p. 87.

[33] H. Å. Gustafsson *et al.*, *Mod. Phys. Lett. A* **3** (1988) 1323.

[34] P. Danielewicz and G. F. Bertsch, *Nucl. Phys* **A533** (1991) 712.

[35] A. Sandoval *el al.*, *Phys. Rev. Lett.* **45** (1980) 874.

[36] R. Brockmann *el al.*, *Phys. Rev. Lett.* **53** (1984) 2015.

[37] J. V. Geaga *el al.*, *Phys. Rev. Lett.* **45** (1980) 1993.

[38] A. M. Baldin *el al.*, Joint Institute for Nuclear Research Report JINR P1-11302,
     1978.

[39] P. Danielewicz, *Phys. Rev. C* **42** (1990) 1564.

[40] G. Batko, J. Randrup, and T. Vetter, *Nucl. Phys.* **A536** (1992) 786;
     *ibid* **A546** (1992) 761.

[41] S. Mrówczyński, *Phys. Rev. C* **32** (1985) 1784.

[42] A. Bonasera and F. Gulminelli, *Phys. Lett. B* **275** (1992) 24.

[43] P. Danielewicz and Q. Pan, *Phys. Rev. C* **46** (1992) 2002.

[44] K. G. R. Doss *et al.*, *Mod. Phys. Lett. A* **3** (1988) 849.

[45] J. Chiba, private communication.,